Article

Immunity

Bile acids modified by the intestinal microbiota promote colorectal cancer growth by suppressing CD8$^+$ T cell effector functions

Graphical abstract

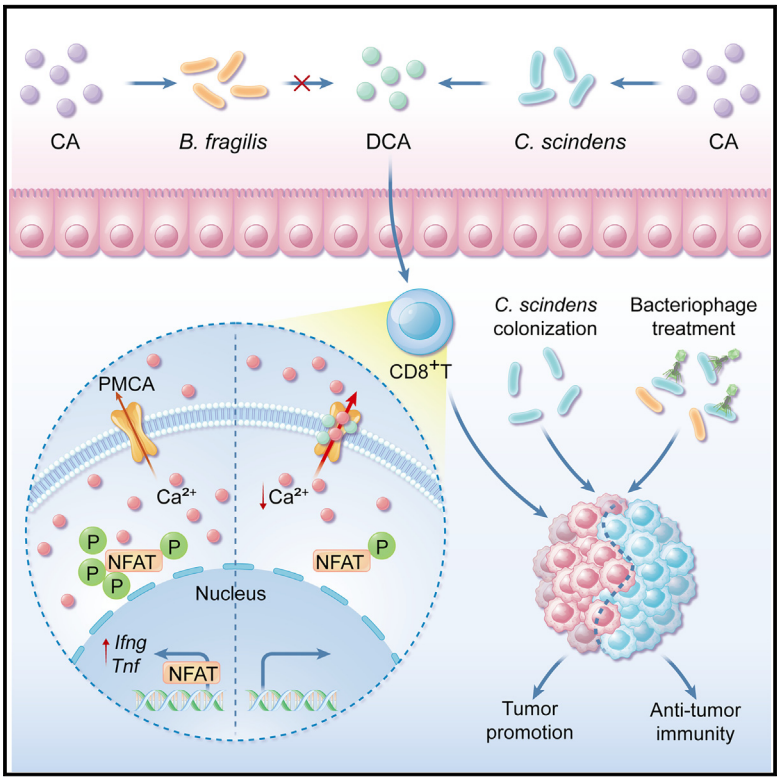

Highlights

- DCA suppresses anti-tumor CD8$^+$ T cell immune responses
- DCA diminishes Ca^{2+}-NFAT2 signaling by potentiating PMCA activity
- DCA concentration negatively correlates with CD8$^+$ T cell function in CRC patients
- Targeting microbial DCA metabolism prevents CRC development in mice

Authors

Jingjing Cong, Pianpian Liu, Zili Han, ..., Linfeng Sun, Wen Pan, Shu Zhu

Correspondence

wenpan@ustc.edu.cn (W.P.), zhushu@ustc.edu.cn (S.Z.)

In brief

Our understanding of the impact of microbial metabolites on anti-tumor immunity is incomplete. Cong et al. show aberrant elevation of the microbiota-derived secondary bile acid, deoxycholic acid, in colorectal cancer patients. Deoxycholic acid suppresses cytotoxic CD8$^+$ T cell effector functions by impairing intracellular calcium accumulation, subsequently promoting colorectal tumor growth.

Cong et al., 2024, Immunity 57, 876–889
April 9, 2024 © 2024 Elsevier Inc. All rights reserved.
https://doi.org/10.1016/j.immuni.2024.02.014

CellPress

CellPress

Immunity

Article

Bile acids modified by the intestinal microbiota promote colorectal cancer growth by suppressing CD8$^+$ T cell effector functions

Jingjing Cong,[1,2,3,11] Pianpian Liu,[1,2,11] Zili Han,[1,2,11] Wei Ying,[1] Chaoliang Li,[1,2] Yifei Yang,[1,4] Shuling Wang,[5] Jianbo Yang,[1,2] Fei Cao,[6] Juntao Shen,[7] Yu Zeng,[1] Yu Bai,[5] Congzhao Zhou,[1] Lilin Ye,[8] Rongbin Zhou,[1] Chunjun Guo,[9] Chunlei Cang,[1] Dennis L. Kasper,[10] Xinyang Song,[6] Lei Dai,[7] Linfeng Sun,[1] Wen Pan,[1,2,*] and Shu Zhu[1,2,4,12,*]

[1]Key Laboratory of Immune Response and Immunotherapy, Center for Advanced Interdisciplinary Science and Biomedicine of IHM, School of Basic Medical Sciences, Division of Life Sciences and Medicine, University of Science and Technology of China, Hefei, China

[2]Department of Digestive Disease, The First Affiliated Hospital of University of Science and Technology of China, Division of Life Sciences and Medicine, University of Science and Technology of China, Hefei 230027, China

[3]School of Pharmacy, Inflammation and Immune Mediated Diseases Laboratory of Anhui Province, Anhui Medical University, Hefei 230032, China

[4]School of Data Science, University of Science and Technology of China, Hefei 230027, China

[5]Department of Gastroenterology, Changhai Hospital, Naval Medical University, Shanghai 200433, China

[6]Shanghai Institute of Biochemistry and Cell Biology, Center for Excellence in Molecular Cell Science, Chinese Academy of Sciences, University of Chinese Academy of Sciences, Shanghai 200031, China

[7]CAS Key Laboratory of Quantitative Engineering Biology, Shenzhen Institute of Synthetic Biology, Shenzhen Institute of Advanced Technology, Chinese Academy of Sciences, Shenzhen 518055, China

[8]Institute of Immunology, Third Military Medical University, Chongqing 400038, China

[9]Jill Roberts Institute for Research in Inflammatory Bowel Disease, Weill Cornell Medicine, Cornell University, New York, NY 10021, USA

[10]Department of Immunology, Blavatnik Institute, Harvard Medical School, Boston, MA 02115, USA

[11]These authors contributed equally

[12]Lead contact

*Correspondence: wenpan@ustc.edu.cn (W.P.), zhushu@ustc.edu.cn (S.Z.)

https://doi.org/10.1016/j.immuni.2024.02.014

SUMMARY

Concentrations of the secondary bile acid, deoxycholic acid (DCA), are aberrantly elevated in colorectal cancer (CRC) patients, but the consequences remain poorly understood. Here, we screened a library of gut microbiota-derived metabolites and identified DCA as a negative regulator for CD8$^+$ T cell effector function. Mechanistically, DCA suppressed CD8$^+$ T cell responses by targeting plasma membrane Ca^{2+} ATPase (PMCA) to inhibit Ca^{2+}-nuclear factor of activated T cells (NFAT)2 signaling. In CRC patients, CD8$^+$ T cell effector function negatively correlated with both DCA concentration and expression of a bacterial DCA biosynthetic gene. Bacteria harboring DCA biosynthetic genes suppressed CD8$^+$ T cells effector function and promoted tumor growth in mice. This effect was abolished by disrupting bile acid metabolism via bile acid chelation, genetic ablation of bacterial DCA biosynthetic pathway, or specific bacteriophage. Our study demonstrated causation between microbial DCA metabolism and anti-tumor CD8$^+$ T cell response in CRC, suggesting potential directions for anti-tumor therapy.

INTRODUCTION

CD8$^+$ T cells are effector lymphocytes with a role in resisting cancers including colorectal cancer (CRC) because of their ability to secret cytokines interferon (IFN)-γ and tumor necrosis factor (TNF)-α, as well as their ability to kill tumor cells. CD8$^+$ T cell activation and effector function involve cytosolic Ca^{2+}-dependent signal transduction mechanisms.[1–3] Nuclear factor of activated T cells (NFAT)2, a Ca^{2+}-dependent transcription factor, regulates expression of genes that direct the effector function of CD8$^+$ T cells.[4–6] The phosphorylated (inactive) form of NFAT2 is located in the cytosol. Upon T cell receptor (TCR) stimulation, the rise of cytosolic Ca^{2+} activates phosphatase calcineurin to dephosphorylate the cytosolic NFAT2, leading to its translocation into the nucleus, where it transcriptionally activates multiple effector molecules (e.g., *Ifng* and *Tnf*).[4–6]

The infiltration of CRC cell nests by CD8$^+$ T cells correlates with a better survival of patients.[7] The presence of high levels of infiltrating CD8$^+$CD45RO$^+$ T cells, as well as increased expression of genes encoding CD8, IFN-γ, Granzyme B (GzmB), and granulysin, predict improved prognosis in CRC patients.[8–10] However, intratumoral CD8$^+$ T cells exhibit a dysfunctional phenotype compared with non-tumoral CD8$^+$ T cells in patients with CRC.[11–13] The human intestinal tract harbors huge numbers

 © 2024 Elsevier Inc. All rights reserved.

of microorganisms collectively referred to as the microbiota, with bacteria representing the dominant and diverse component. The intestinal microbiota is closely associated with the development of CRC[14,15]; however, it remains largely unknown whether the intestinal microbiota contributes to dysfunctional $CD8^+$ T cell immune responses in CRC.

The intestinal microbiota produces numerous metabolites, and certain microbial metabolites can influence tumor development and regulate systemic immune responses,[14–16] such as secondary bile acids, which are produced by microbiota through the conversion of primary bile acids.[17,18] Deoxycholic acid (DCA) is the one of the most abundant secondary bile acids in humans, and it is derived from cholic acid (CA) in a process reliant upon a biosynthetic process mediated by *Clostridium* species that contain the bile-acid-induced (*bai*) operon.[19–21] DCA is known to promote CRC through DNA-damaging effects and through disrupting the intestinal mucosal barrier.[22] Clinical studies have reported that DCA concentrations are elevated in the serum and stool of CRC patients.[23,24] Secondary bile acids are also reported to regulate the differentiation of $CD4^+$ T cells.[25,26] These findings have prompted our investigation into the potential of microbial metabolites in modulating $CD8^+$ T cell anti-tumor immune responses, thereby assessing whether manipulation of the microbiota or its metabolites could prove effective anti-tumor therapy.

Here, seeking potential microbial metabolites that may affect dysfunctional $CD8^+$ T cell immune responses in CRC, we screened a panel of microbiota-derived metabolites for their immunomodulatory impact on mouse $CD8^+$ T cells. Our screen identified DCA as a negative regulator of $CD8^+$ T cell-mediated anti-tumor immune responses. This occurred by diminishing Ca^{2+}-NFAT2 signaling in a plasma membrane Ca^{2+} ATPase (PMCA)-dependent manner. The concentrations of DCA and the expression of *bai* operon gene were negatively correlated with the frequencies of GzmB-, IFN-γ-, and TNF-α-expressing cells in CRC patients. The culture supernatant from a *Clostridium scindens* (*C. scindens*) strain harboring the complete *bai* operon, contained DCA and suppressed the effector function of $CD8^+$ T cells. Moreover, colonization of mice with *C. scindens* led to accelerated tumor growth, and this tumor-promoting effect was abolished by bile acids chelation or by bacteriophages that targeted *C. scindens*. Our study uncovered a mechanism that the environmental cue impairs $CD8^+$ T cell function and promotes CRC development.

RESULTS

DCA suppresses the effector function of $CD8^+$ T cells

To determine whether gut microbiota-derived metabolites modulate the effector function of $CD8^+$ T cells, we prepared a library comprising 73 microbiota-derived small molecule compounds (reported to be present in lower concentrations and/or incidence in the germ-free [GF] mice than in the GF mice colonized with microbiota from specific pathogen-free [SPF] mice,[27] Table S1) and tested their impacts on $CD8^+$ T cell-mediated cytotoxicity, or effector function via IFN-γ production. For cytotoxicity-based screening assays, $CD8^+$ T cells were isolated from spleens of ovalbumin (OVA)-specific OT-1 TCR transgenic mice and cultured with individual metabolites from the library under stimulation with anti-CD3/CD28 monoclonal antibodies (mAbs). The pretreated cells were then co-cultured with OVA-expressing B16 (B16-OVA) melanoma cells, and the cytotoxicity of $CD8^+$ T cells was assessed by measuring the survival of target cells using real-time cell index analysis (Figure 1A). For IFN-γ-based screening, $CD8^+$ T cells were isolated from spleens of wild-type (WT) C57BL/6 mice, cultured with individual metabolites from the library under stimulation with anti-CD3/CD28 mAbs, and analyzed by flow cytometry to assess the IFN-γ^+ cell population among $CD8^+$ T cells (Figure 1B). The metabolite indole-3-aldehyde (I3A), which enhances the production of IFN-γ in $CD8^+$ T cells,[28] was used as a positive control (Figure S1A).

Exposure to the secondary bile acid DCA largely decreased the cytotoxicity of $CD8^+$ T cells and the proportions of IFN-γ^+ cells (Figures 1A, 1B, and S1B). Moreover, the suppressive effect of DCA on the expression of GzmB, IFN-γ, and TNF-α in $CD8^+$ T cells was dose-dependent, with the inhibitory effect becoming evident beginning at 150 μM DCA (Figure 1C), a concentration lower than the reported average concentration of this secondary bile acid in the human appendix (200 μM).[29] DCA's suppressive effect was not limited to the initial phase of T cell activation, as DCA still inhibited the expression of GzmB, IFN-γ, and TNF-α in $CD8^+$ T cells that had undergone pre-activation and subsequent rest (Figure S1C). Consistent with our observations for impaired production of effector molecules, DCA inhibited the activation of $CD8^+$ T cells as evidenced by decreased expression of surface markers CD69, CD25, and CD44 (Figure 1D). DCA also inhibited the proliferation capacity of $CD8^+$ T cells, again in a dose-dependent manner (Figures 1E and 1F). These results demonstrated that DCA suppresses the activation, proliferation, and effector function of $CD8^+$ T cells. Additionally, DCA exerted a similar immunosuppressive effect on $CD4^+$ T cells, as demonstrated by lower expression of IFN-γ, TNF-α, CD69, CD25, and CD44 upon exposure to DCA (Figures S1D and S1E).

We then evaluated the impact of other secondary bile acids, including lithocholic acid (LCA), 3-oxo-CA, 7-oxo-DCA, 12-oxo-CA, tauroursodeoxycholic acid (TUDCA), and glycodeoxycholic acid (GDCA), on the effector function of $CD8^+$ T cells. LCA suppressed the expression of GzmB, IFN-γ, and TNF-α in $CD8^+$ T cells, while no significant immunosuppressive effects were observed with the other secondary bile acids (Figure S1F).

We next assessed whether the observed impact of DCA on the effector function of $CD8^+$ T cells might be caused by DCA-induced death of these cells, since bile acids have detergent properties at high concentrations (>400 μM),[17] which can lead to cell death.[30] Although DCA exhibited a mild cytotoxic effect on $CD8^+$ T cells (Figure S1G), the idea of a simple detergent-mediated mechanism was excluded by assays showing that SDS treatment (60 μM, the cytotoxic effect of SDS at this concentration was similar to DCA at 250 μM) did not evoke the same extent of decline in effector molecule expression in $CD8^+$ T cell compared with DCA treatment (Figure S1H).

Moreover, we excluded regulated cell death mechanisms from DCA's effects in experiments using the chemical caspase-3 inhibitor Ac-DEVD-CHO or genetic knockout strains including *Rip3*$^{-/-}$, *Caspase-1*$^{-/-}$, *Caspase-11*$^{-/-}$, *Gsdme*$^{-/-}$, and

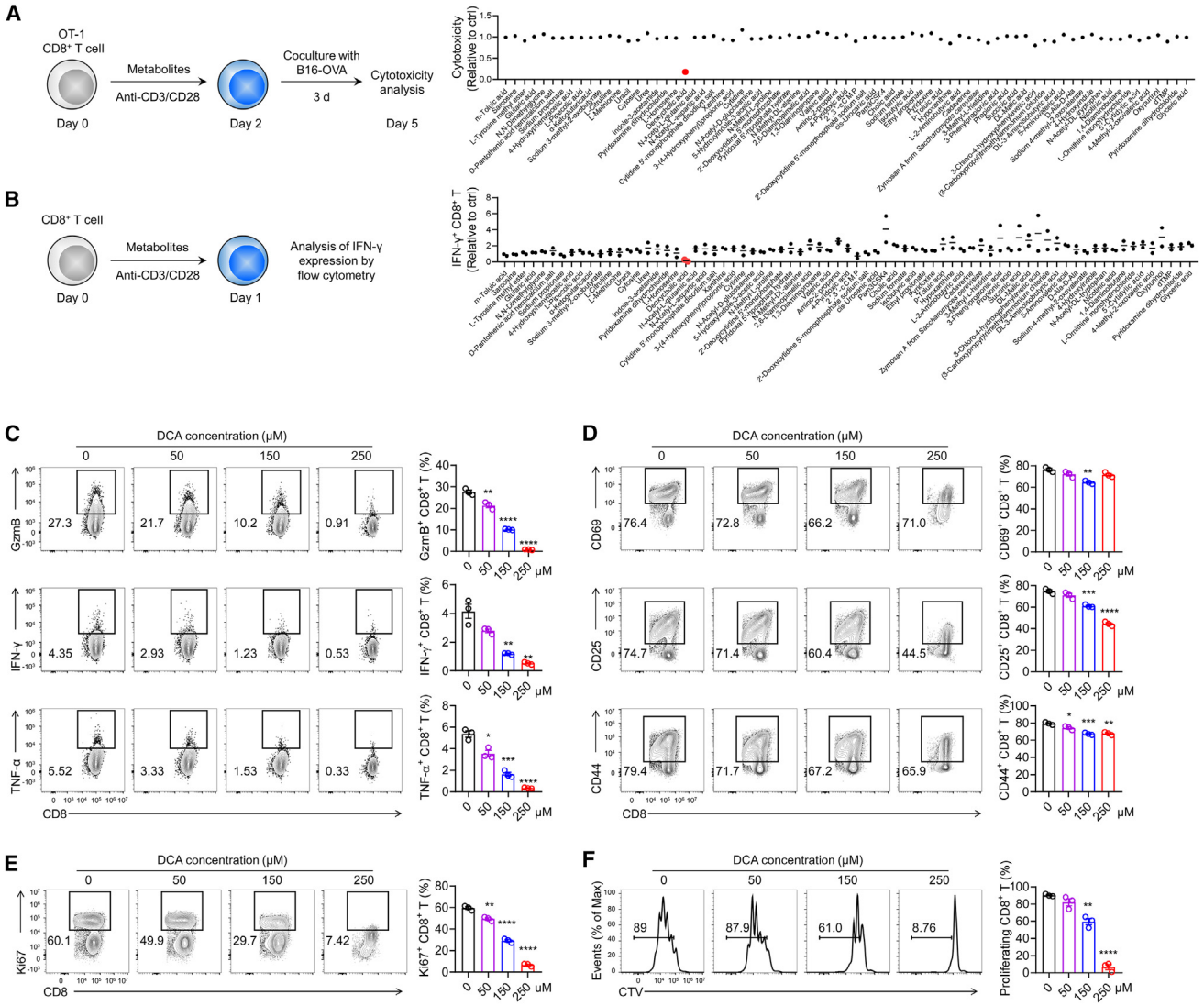

Figure 1. DCA suppresses the effector function of CD8$^+$ T cells

(A) Schematic screening procedure (left): splenic CD8$^+$ T cells from OT-1 mice were treated with 73 bacteria-derived metabolites (500 μM) or solvent control for 48 h. Scatter plots (right) displaying the cytotoxicity of CD8$^+$ T cells against B16-OVA target cells.

(B) Schematic screening procedure (left): splenic CD8$^+$ T cells were treated with 73 bacteria-derived metabolites (500 μM) or solvent control for 24 h. Scatterplots (right) displaying fold change in the proportions of IFN-γ$^+$ cells among CD8$^+$ T cells; n = 2. Data are pooled from two independent experiments.

(C–E) Splenic CD8$^+$ T cells were treated with DCA at the indicated concentrations for 24 h (C) or 48 h (D and E). Representative flow cytometry plots and quantification of GzmB$^+$, IFN-γ$^+$, TNF-α$^+$ (C), CD69$^+$, CD25$^+$, CD44$^+$ (D), and Ki67$^+$ (E) cells among CD8$^+$ T cells; n = 3. The experiment was repeated at least three times.

(F) Splenic CD8$^+$ T cells were treated with DCA at the indicated concentrations for 72 h. Representative flow cytometry profiles and percentages of proliferating CD8$^+$ T cells; n = 3. Data are pooled from three independent experiments.

Data are shown as mean ± SEM (C–F). Statistics are analyzed by one-way ANOVA (C–F); *p < 0.05, **p < 0.01, ***p < 0.001, and ****p < 0.0001.

See also Figure S1 and Table S1.

Gsdmd$^{-/-}$ mice, to specifically block the necroptosis, apoptosis, or pyroptosis in the cells (Figures S1I and S1J). Both Ac-DEVD-CHO treatment or *Gsdmd* deficiency increased the viability of CD8$^+$ T cells in the presence of DCA; however, neither condition enhanced the expression of GzmB or IFN-γ by CD8$^+$ T cells (Figures S1I and S1J). These results demonstrated that cell death cannot account for the observed impact of DCA exposure in suppressing the effector function of CD8$^+$ T cells.

Secondary bile acids exert functions through their interactions with receptors, including GPBAR1, FXR, and VDR.[31] We therefore investigated whether these receptors are involved in DCA-mediated inhibition of CD8$^+$ T cell effector function. Accordingly, splenic CD8$^+$ T cells were isolated from *Gpbar1*$^{-/-}$, *Fxr*$^{-/-}$, *Vdr*$^{-/-}$, and *Fxr*$^{-/-}$*Vdr*$^{-/-}$ mice, and the cells were treated with DCA. GzmB and IFN-γ production by CD8$^+$ T cells was still decreased by DCA treatment in these mice strains (Figure S1K),

indicating that GPBAR1, FXR, or VDR do not substantially contribute to the suppressive effect of DCA on $CD8^+$ T cell effector function. Taken together, these data suggested that DCA suppresses the activation, proliferation, effectors production, and killing function of $CD8^+$ T cells, in a cell death and known receptors independent way.

DCA suppresses $CD8^+$ T cell effector function by inhibiting Ca^{2+}-NFAT2 signaling

$CD8^+$ T cell activation and effector function involve cytosolic Ca^{2+}-dependent signal transduction mechanisms.[1–3] Therefore, aberrant accumulation of cytosolic Ca^{2+} concentrations may lead to the observed DCA-mediated inhibition of $CD8^+$ T cell effector function. Pursuing this, we monitored cytosolic Ca^{2+} flux by measuring the fluorescence of a Ca^{2+}-sensitive dye (Fura-2, AM). The real-time fluorescence intensity data for anti-CD3/CD28 activated-$CD8^+$ T cells showed that DCA inhibited ionomycin-induced cytosolic Ca^{2+} accumulation (Figures 2A and S2A). The basal Ca^{2+} flux in resting $CD8^+$ T cells was not influenced by DCA (Figure S2B). To ensure that inhibition of cytosolic Ca^{2+} accumulation by DCA was not due to differences in T cell activation, we pre-activated the $CD8^+$ T cells, subsequently allowed them to rest, and then treated them with DCA. Even under these conditions, DCA continued to inhibit the cytosolic Ca^{2+} accumulation (Figure 2B). DCA also inhibited the ionomycin-induced cytosolic Ca^{2+} accumulation in $CD4^+$ T cells (Figure S2C). Among other secondary bile acids tested, LCA exhibited inhibitory effects on ionomycin-induced cytosolic Ca^{2+} accumulation in $CD8^+$ T cells, whereas GDCA and TUDCA did not (Figure S2D).

NFAT2, a transcription factor activated by increased cytosolic Ca^{2+}, governs the effector function of $CD8^+$ T cells.[4–6] Immunoblotting showed that DCA treatment of anti-CD3/CD28 activated-$CD8^+$ T cells decreased nuclear localization of NFAT2 (Figure 2C). A similar decrease was observed in phorbol 12-myristate 13-acetate (PMA)/ionomycin-activated Jurkat cells (Figure 2C). To assay the effect of DCA on NFAT2's transcriptional activity, we used NFAT2-luciferase reporter containing NFAT2-responsive elements that drive the transcription of the firefly luciferase and observed that PMA/ionomycin stimulation increased NFAT2-luciferase reporter activity—to a level 6-fold over baseline in DMSO-treated Jurkat cells—but found this induction was weakened by DCA (Figure 2D). Together, these results demonstrated that DCA inhibits Ca^{2+} flux-induced nuclear translocation of NFAT2 and NFAT2-mediated transcription.

We next constructed a plasmid (ΔCaM-AI) encoding a Ca^{2+}-independent, constitutively active form of calcineurin, which leads to constitutive activation of NFAT2.[32] Jurkat cells transfected with the ΔCaM-AI plasmid no longer displayed the DCA-mediated suppression of NFAT2 nuclear translocation and transcriptional activity, as well as the mRNA levels of *IFNG* and *TNF* (Figures 2E–2G). These results suggested that the observed DCA inhibition of $CD8^+$ T cell effector function is dependent upon impairing Ca^{2+}-NFAT2 signaling.

DCA inhibits Ca^{2+}-NFAT2 signaling in a PMCA-dependent manner

We next assessed whether the observed impacts of DCA on the reduced accumulation of cytosolic Ca^{2+} may involve DCA-Ca^{2+} chelation since calcium preferentially binds to secondary bile acids including DCA in the small intestine.[33] However, the addition of DCA did not reduce free Ca^{2+} in cell-free medium (Figure S2E), suggesting that DCA does not chelate Ca^{2+}, and this is not the mechanism of the DCA-mediated suppression of cytosolic Ca^{2+} accumulation.

The cytosolic Ca^{2+} concentration reflects a coordinated balance between Ca^{2+} movement across the plasma membrane and intracellular stores.[1] TCR stimulation initiates a cascade of phosphorylation of proximal TCR signaling molecules (Src, Zap70, LAT, and PLCγ1), which leads to Ca^{2+} release from the endoplasmic reticulum (ER) and subsequent store-operated calcium entry (SOCE).[1] The SOCE through the Ca^{2+} release-activated Ca^{2+} (CRAC) channels stands as the predominant Ca^{2+} influx pathway in lymphocytes and plays a pivotal role in the anti-tumor immunity mediated by $CD8^+$ T cells.[1,2] DCA did not affect expressions of pSrc, pZap70, pLAT, or pPLCγ1 in $CD8^+$ T cells (Figure S2F). Moreover, the presence of the selective CRAC channel blocker BTP2 did not reverse the immunosuppressive effect of DCA on $CD8^+$ T cells (Figure S2G).

PMA/ionomycin stimulation triggers Ca^{2+} release directly from the ER in a transporter independent manner and induces T cell production of effector molecules in a PLCγ1-independent manner.[34] Under stimulation with PMA/ionomycin, DCA still inhibited both the nuclear translocation and the transcriptional activity of NFAT2 and decreased the expression of effector molecules (Figures 2C, 2D, 2G, and S2H). These findings indicated that DCA-driven defects in cytosolic Ca^{2+} accumulation are not a consequence of reduced extracellular Ca^{2+} influx or Ca^{2+} release from the ER. Rather, there is possible enhanced Ca^{2+} efflux across the plasma membrane or return to intracellular stores.

We therefore focused on several Ca^{2+} channels/pumps that can lower cytosolic Ca^{2+} concentrations, including: (1) PMCA, which can pump Ca^{2+} from cytosol to the extracellular space; (2) sarcoplasmic/endoplasmic reticulum Ca^{2+} ATPases (SERCAs), which can pump Ca^{2+} from cytosol to the ER; and (3) mitochondrial Ca^{2+} uniporter (MCU), which can conduct Ca^{2+} from cytosol to mitochondria.[1,3] We next investigated whether blockade of these channels/pumps restored the effector function of $CD8^+$ T cells. The PMCA inhibitor $LaCl_3$ increased the expression of IFN-γ and TNF-α, cytotoxicity, and the nuclear translocation of NFAT2 in DCA-treated $CD8^+$ T cells (Figures 3A–3C), whereas blockade of SERCA or MCU had no effect (Figure 3A). A similar rescue effect was also observed when using short hairpin RNA (shRNA)-mediated silencing of *PMCA4*, which is the PMCA subtype highly expressed in T cells,[35] in Jurkat cells (Figures 3D and 3E). However, the suppressive effect of LCA on $CD8^+$ T cell effector function could not be reversed by $LaCl_3$ (Figure S2I), indicating that LCA's immunosuppressive effect was not dependent on the PMCA-mediated mechanism but might be attributed to its potent cytotoxicity (Figure S2J).[36] We next assessed the effect of DCA on Ca^{2+} efflux using Ca^{2+} extrusion assay. We used SERCA inhibitor thapsigargin (Tg) to deplete ER Ca^{2+} stores in the absence of extracellular Ca^{2+} and then added extracellular Ca^{2+} to 1 mM to increase cytosolic Ca^{2+}. Ca^{2+} extrusion was then estimated upon the subsequent removal of extracellular Ca^{2+}. DCA-treated $CD8^+$ T cells had reduced cytosolic Ca^{2+} after removal of extracellular Ca^{2+}

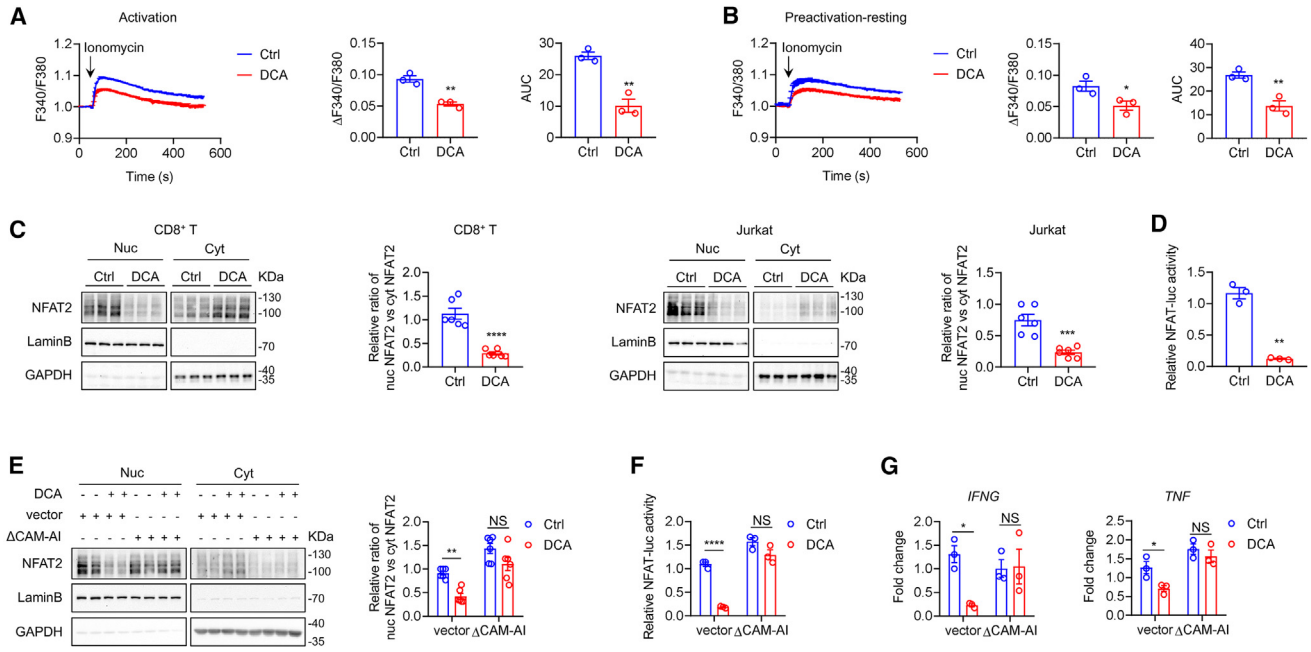

Figure 2. DCA suppresses CD8⁺ T cell effector function by inhibiting Ca^{2+}-NFAT2 signaling

(A) Splenic $CD8^+$ T cells were treated with 150 μM DCA for 24 h. Cytosolic Ca^{2+} were then measured. Plots of real-time F340/F380 ratio (left), maximal increased F340/F380 ratio (middle), and the area under the curve (AUC) relative to the baseline (right) after ionomycin stimulation are shown; n = 3. The experiment was repeated three times.

(B) Splenic $CD8^+$ T cells were stimulated with anti-CD3/CD28 mAbs for 18 h, followed by resting in the culture medium supplemented with 100 U/mL IL-2 for an additional 48 h. The cells were then treated with 150 μM DCA for 48 h. Cytosolic Ca^{2+} were then measured; n = 3. The experiment was repeated twice.

(C) Splenic $CD8^+$ T cells were treated with 150 μM DCA for 24 h; Jurkat cells were treated with 150 μM DCA for 16 h. Immunoblotting of NFAT2; n = 6. Data are pooled from two independent experiments.

(D) Jurkat cells were transfected with NFAT-luciferase reporter plasmids. The cells were then treated with 150 μM DCA for 24 h and assessed with luciferase assays; n = 3. The experiment was repeated three times.

(E) Jurkat cells were transfected with ΔCaM-AI or empty vector. The cells were then treated with 150 μM DCA for 24 h. Immunoblotting of NFAT2; n = 6. Data are pooled from three independent experiments.

(F) Jurkat cells were co-transfected with NFAT-luciferase reporter plasmids and ΔCaM-AI or empty vector. The cells were then treated with 150 μM DCA for 24 h and assessed with luciferase assays; n = 3. The experiment was repeated at least three times.

(G) Jurkat cells were transfected with ΔCaM-AI or empty vector. The cells were then treated with 150 μM DCA for 24 h and assessed the mRNA levels of *IFNG* and *TNF* by quantitative reverse-transcription PCR; n = 3. The experiment was repeated three times.

Data are shown as mean ± SEM (A–G). Statistics are analyzed by unpaired t test (A–D), and two-way ANOVA (E–G); *p < 0.05, **p < 0.01, ***p < 0.001, and ****p < 0.0001. NS, not significant.

See also Figure S2.

(Figure 3F). These results suggested that DCA potentiated PMCA-mediated Ca^{2+} efflux to suppress cytosolic Ca^{2+} accumulation.

The transport of Ca^{2+} through transporters is governed by both the concentration gradient of Ca^{2+} across the biological membrane and the membrane potential. To elucidate the potential impact of DCA on the membrane potential of T cells, we utilized whole-cell patch clamp recordings in the current-clamp mode, and found that DCA did not impact the T cell membrane potential (Figures S2K and S2L).

To further investigate the connection between DCA and PMCA, we performed coimmunoprecipitation using biotin-labeled DCA and then pull down with streptavidin beads. We found strong interaction between DCA and both human PMCA4 and mouse PMCA4 (Figure 3G).[35] We then performed surface plasmon resonance (SPR) using purified human PMCA4 (which is highly conserved to mouse PMCA4) protein produced by HEK293F cells (Figures S2M and S2N).[37] DCA exhibited a robust binding affinity to PMCA4 (equilibrium dissociation constant, K_D = 688 nM; Figure 3H). LCA showed weak binding to PMCA4 (K_D = 119 μM; Figure S2O). GDCA and TUDCA did not bind to PMCA4 in the SPR assay (Figure S2O). These observations were consistent with the findings that the suppressive effect of LCA on $CD8^+$ T cell effector function could not be reversed by $LaCl_3$ and that GDCA and TUDCA did not impact effector function and Ca^{2+} flux in $CD8^+$ T cells. These results suggested the important role of the DCA-PMCA4 binding in DCA-mediated inhibition of $CD8^+$ T cell effector function and Ca^{2+} signaling.

Next, we measured the effect of DCA on the ATPase activity of purified PMCA4 protein. Purified SERCA protein was used as a control (Figure S2N). The addition of DCA promoted the ATPase activity of PMCA4 (by ~50%), but did not enhance the ATPase activity of SERCA (Figure 3I).

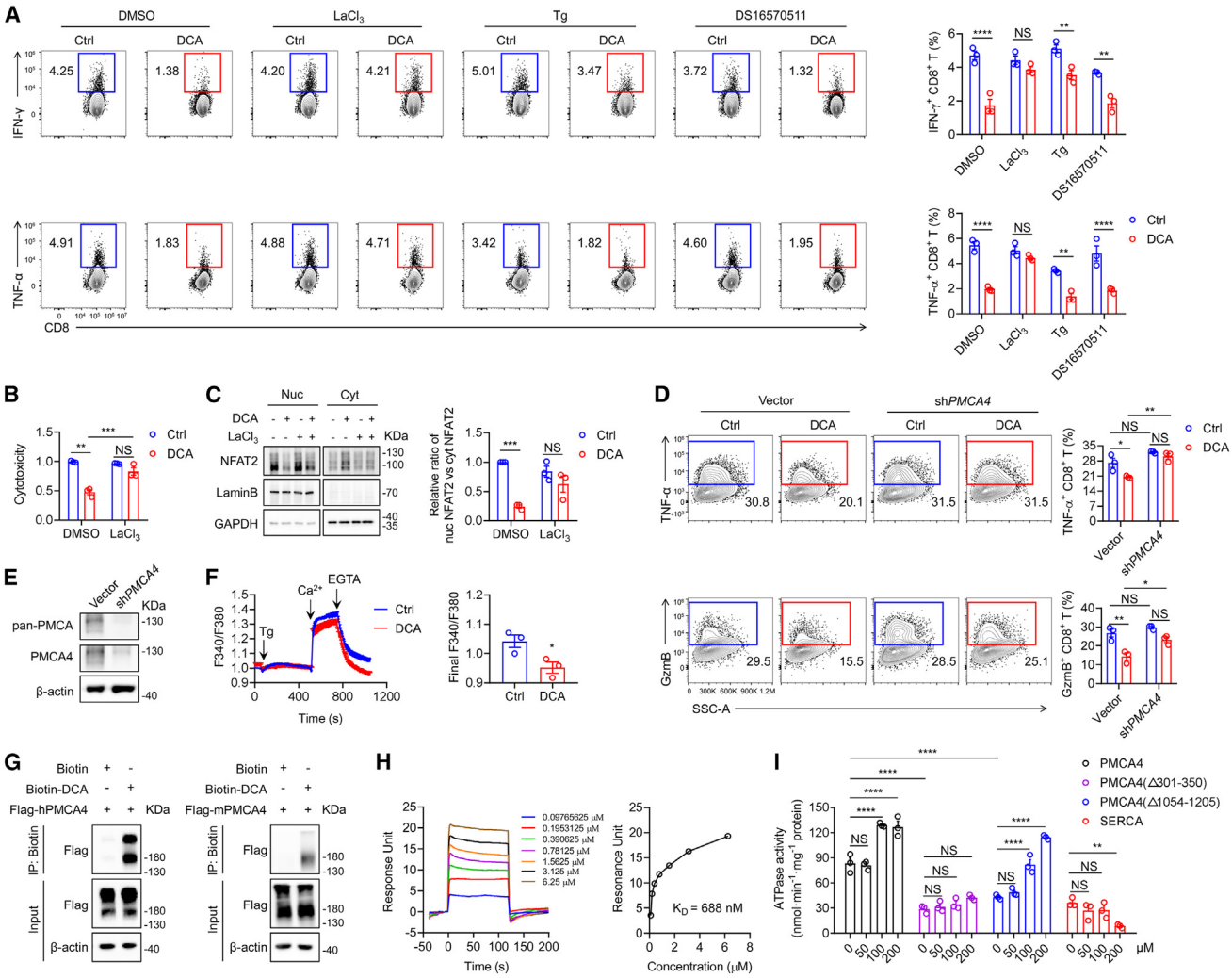

Figure 3. DCA inhibits Ca^{2+}-NFAT2 signaling in a PMCA-dependent manner

(A) Splenic $CD8^+$ T cells were treated with 150 μM DCA, with or without $LaCl_3$ (60 μM), Tg (5 nM), and DS16570511 (25 μM), for 24 h. Representative flow cytometry plots and quantification of IFN-γ^+ and TNF-α^+ cells among $CD8^+$ T cells; n = 3. The experiment was repeated three times.

(B) Splenic $CD8^+$ T cells from OT-1 mice were treated with 150 μM DCA, with or without $LaCl_3$ (60 μM) for 48 h. Scatterplots displaying the cytotoxicity of $CD8^+$ T cells against target cells; n = 3. The experiment was repeated twice.

(C) Splenic $CD8^+$ T cells were treated with 150 μM DCA, with or without $LaCl_3$ (60 μM), for 24 h. Immunoblotting of NFAT2; n = 3. Data are pooled from three independent experiments.

(D and E) The *PMCA4* gene in Jurkat cells was silenced using a lentiviral vector. The lentivirus-infected Jurkat cells were sorted and subsequently treated with 50 μM DCA for 24 h, and PMA/ionomycin (0.08/1.3 μM) plus protein transport inhibitors were added to the cells during the last 4 h. Quantification of the proportions of TNF-α^+ and $GzmB^+$ cells (D); n = 3. Immunoblotting of pan-PMCA and PMCA4 expression in the infected Jurkat cells (E).

(F) Splenic $CD8^+$ T cells were treated with 150 μM DCA for 24 h. Cytosolic Ca^{2+} were then measured. Plots of real-time F340/F380 ratio (left) and the final cytosolic Ca^{2+} after addition of EGTA (right) are shown; n = 3. The experiment was repeated three times.

(G) 293T cells were transfected with PMCA4. The cell lysates were incubated with biotin-labeled DCA and then pulled down with streptavidin beads. The samples were then immunoblotted with anti-FLAG mAb. The experiment was repeated three times.

(H) The human PMCA4 protein was immobilized on the chip and was tested for binding with gradient concentrations of DCA by SPR. Binding kinetics and K_D of DCA with PMCA4 are shown. The experiment was repeated three times.

(I) Full-length human PMCA4, SERCA, and two PMCA4 truncation mutants were incubated in the ATPase reaction medium in the presence of DCA at the indicated concentrations. ATPase activities of these proteins are shown; n = 3. The experiment was repeated twice.

Data are shown as mean ± SEM (A–D, F, and I). Statistics are analyzed by unpaired t test (F) and two-way ANOVA (A–D and I); *p < 0.05, **p < 0.01, ***p < 0.001, and ****p < 0.0001. NS, not significant.

See also Figure S2.

Biochemical characterizations of the PMCA family proteins in human suggest two regions essential to the transport activity: a juxtamembrane domain with lipid binding loop between TM2 and TM3 (301–350),[38–42] and the carboxyl-terminal auto-inhibitory domain (1,054–1,205).[39–45] We generated two truncation mutants lacking each domain (Figure S2N), and measured their

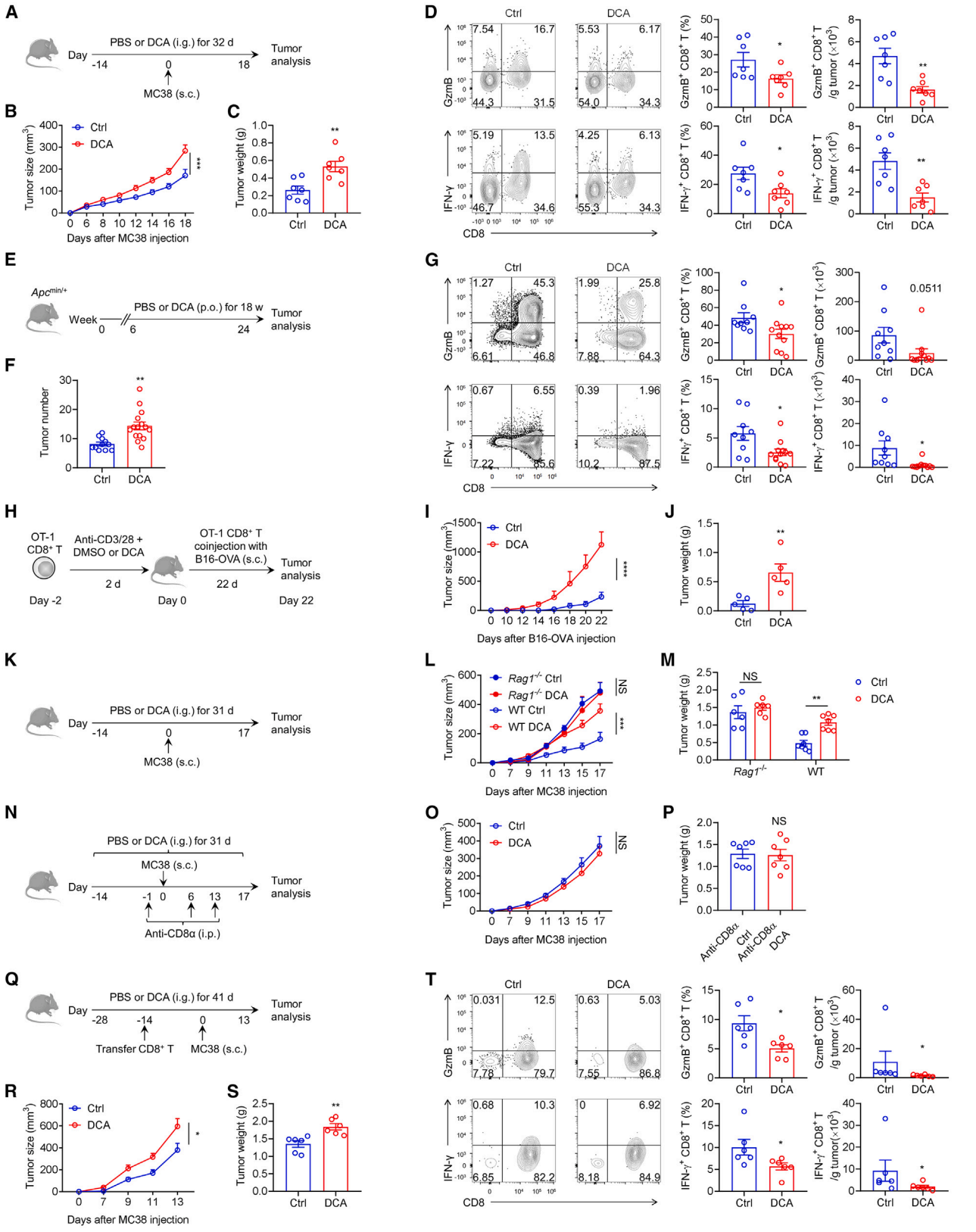

(legend on next page)

ATPase activities. Deleting the lipid binding loop or the C terminus impaired the ATPase activity of PMCA4 (Figure 3I). This was distinct from the auto-inhibitory role of C terminus previously reported for long isoforms of human PMCAs.[42] Although addition of DCA could still promote the ATPase activity of the C terminus truncation mutant of PMCA4 (by a similar fold compared with the full-length PMCA4), DCA had no effect on the activity of the lipid binding loop truncation mutant (Figure 3I). Taken together, these results suggested that DCA impairs the effector function of $CD8^+$ T cells by preventing cytosolic Ca^{2+} accumulation, specifically by potentiating PMCA-mediated Ca^{2+} efflux.

DCA promotes tumor growth by suppressing the anti-tumor $CD8^+$ T cell immune responses

We next investigated the impacts of DCA on $CD8^+$ T cells *in vivo*. Mice administered DCA daily by oral gavage for 2 weeks (Figure S3A) exhibited elevated DCA concentrations in both their serum and stool (Figure S3B). This administration reduced the proportions and counts of IFN-γ^+ and TNF-α^+ cells among $CD8^+$ T cells in the small intestinal epithelium, large intestinal epithelium, mesenteric lymph node (mLN), and spleen (Figures S3C–S3G). However, DCA displayed minimal to no immunosuppressive effect on $CD4^+$ T cells in these tissues (Figures S3D–S3G). The total cell counts of $CD8^+$ T cells and $CD4^+$ T cells were generally not reduced by DCA across these tissues, except for the small intestine epithelium (Figures S3D–S3G). Intraperitoneal injection of mice with DCA daily for 2 weeks (Figure S3H) also increased serum and fecal DCA concentrations (Figure S3I) and reduced the expression of IFN-γ and TNF-α in splenic $CD8^+$ T cells (Figure S3J), but DCA did not affect the counts of total T cells or the ratio of $CD8^+$ T cells and $CD4^+$ T cells in the spleen (Figure S3K). Moreover, DCA treatment did not affect the development of double-negative ($CD4^-CD8^-$) progenitors, double-positive ($CD4^+CD8^+$), or CD4 or CD8 single-positive thymocytes (Figure S3L). Taken together, these results supported that DCA impairs the cytokine production of $CD8^+$ T cells but does not affect T cell development *in vivo*.

To confirm the involvement of proposed PMCA-Ca^{2+} mechanism in DCA-mediated suppression of $CD8^+$ T cells effector function *in vivo*, we isolated splenic $CD8^+$ T cells from the mice gavaged with either PBS or DCA, stimulated them with anti-CD3/CD28 mAbs, and then assessed their Ca^{2+} flux and effector function (Figure S3M). $CD8^+$ T cells isolated from DCA-exposed mice exhibited impaired ionomycin-induced cytosolic Ca^{2+} accumulation and decreased expression of IFN-γ and TNF-α (Figures S3N and S3O). This impairment was rescued by the addition of $LaCl_3$ (Figures S3N and S3O). These results suggested that DCA suppresses the production of effector molecules by $CD8^+$ T cells through a PMCA-dependent pathway in an *in vivo* context.

Given that $CD8^+$ T cells function in tumor immunosurveillance, we speculated that DCA's inhibition of $CD8^+$ T cell effector function may promote CRC development by impairing the anti-tumor $CD8^+$ T cell response. Pursuing this, we chose two CRC mouse models: a MC38 syngeneic transplant model and an $Apc^{min/+}$ spontaneous model.[46] WT mice were given DCA daily by oral gavage or intraperitoneal injection and were subcutaneously injected with MC38 colon tumor cells after 2 weeks of DCA administration (Figures 4A and S4C). The metabolite I3A, which inhibits tumor growth through promoting $CD8^+$ T cells production of IFN-γ,[28] was used as a positive control (Figures S4H–S4K). Either oral or intraperitoneal administration of DCA accelerated tumor development, compared with the PBS-treated group (Figures 4B, 4C, S4D, and S4E). Moreover, we detected lower proportions and cell counts of tumor-infiltrating $CD8^+$ T cells expressing GzmB and IFN-γ in the DCA-exposed mice (Figures 4D and S4F). We also observed a slight decrease in the proportions and a significant decrease in the cell counts of tumor-infiltrating

Figure 4. DCA promotes tumor growth by suppressing anti-tumor $CD8^+$ T cell immune responses

(A) Schematic experimental procedure in (B)–(D): WT mice were gavaged with DCA or PBS daily for 32 days and were injected (subcutaneously [s.c.]) with MC38 cells on day 0.

(B and C) Tumor growth curves (B) and tumor weight (C) at 18 days after MC38 inoculation; n = 7. The experiment was repeated three times.

(D) Representative flow cytometry plots and quantification of $GzmB^+$ and IFN-γ^+ cells among $CD8^+$ T cells; n = 7. The experiment was repeated twice.

(E) Schematic experimental procedure in (F) and (G): $Apc^{min/+}$ mice were fed with DCA-containing or normal drinking water from 6 weeks of age.

(F) Tumor number at week 24; n = 11–15. Data are pooled from two independent experiments.

(G) Representative flow cytometry plots and quantification of $GzmB^+$ and IFN-γ^+ cells among $CD8^+$ T cells; n = 9–11. Data are pooled from two independent experiments.

(H) Schematic experimental procedure in (I) and (J): splenic $CD8^+$ T cells from OT-1 mice were treated with 150 μM DCA for 48 h. The pretreated $CD8^+$ T cells and B16-OVA cells were then co-injected (s.c.) into $Rag1^{-/-}$ mice on day 0.

(I and J) Tumor growth curves (I) and tumor weight (J) at 22 days after B16-OVA inoculation; n = 5. The experiment was repeated three times.

(K) Schematic experimental procedure in (L) and (M): WT and $Rag1^{-/-}$ mice were gavaged with DCA or PBS daily for 31 days and were injected (s.c.) with MC38 cells on day 0.

(L and M) Tumor growth curves (L) and tumor weight (M) at 17 days after MC38 inoculation; n = 6–7. The experiment was repeated twice.

(N) Schematic experimental procedure in (O) and (P): WT mice were gavaged with DCA or PBS daily for 31 days and were injected (intraperitoneally [i.p.]) with anti-CD8α mAb weekly. The mice were then injected (s.c.) with MC38 cells on day 0.

(O and P) Tumor growth curves (O) and tumor weight (P) at 17 days after MC38 inoculation; n = 7. The experiment was repeated three times.

(Q) Schematic experimental procedure in (R)–(T): splenic $CD8^+$ T cells were transferred into $Rag1^{-/-}$ recipient mice that received gavage with DCA or PBS for 14 days. The $Rag1^{-/-}$ recipient mice continued to receive gavage with DCA or PBS for an additional 27 days and were injected (s.c.) with MC38 cells on day 0.

(R and S) Tumor growth curves (R) and tumor weight (S) at 13 days after MC38 inoculation; n = 6.

(T) Representative flow cytometry plots and quantification of $GzmB^+$ and IFN-γ^+ cells among $CD8^+$ T cells; n = 6.

Each symbol in (C), (D), (F), (G), (J), (M), (P), (S), and (T) represents measurement from an individual mouse. Data are shown as mean ± SEM (B–D, F, G, I, J, L, M, O, P, and R–T). Statistics are analyzed by two-way ANOVA (B, I, L, M, O, and R) and unpaired t test (C, D, F, G, J, P, S, and T); $^*p < 0.05$, $^{**}p < 0.01$, $^{***}p < 0.001$, and $^{****}p < 0.0001$. NS, not significant.

See also Figures S3 and S4.

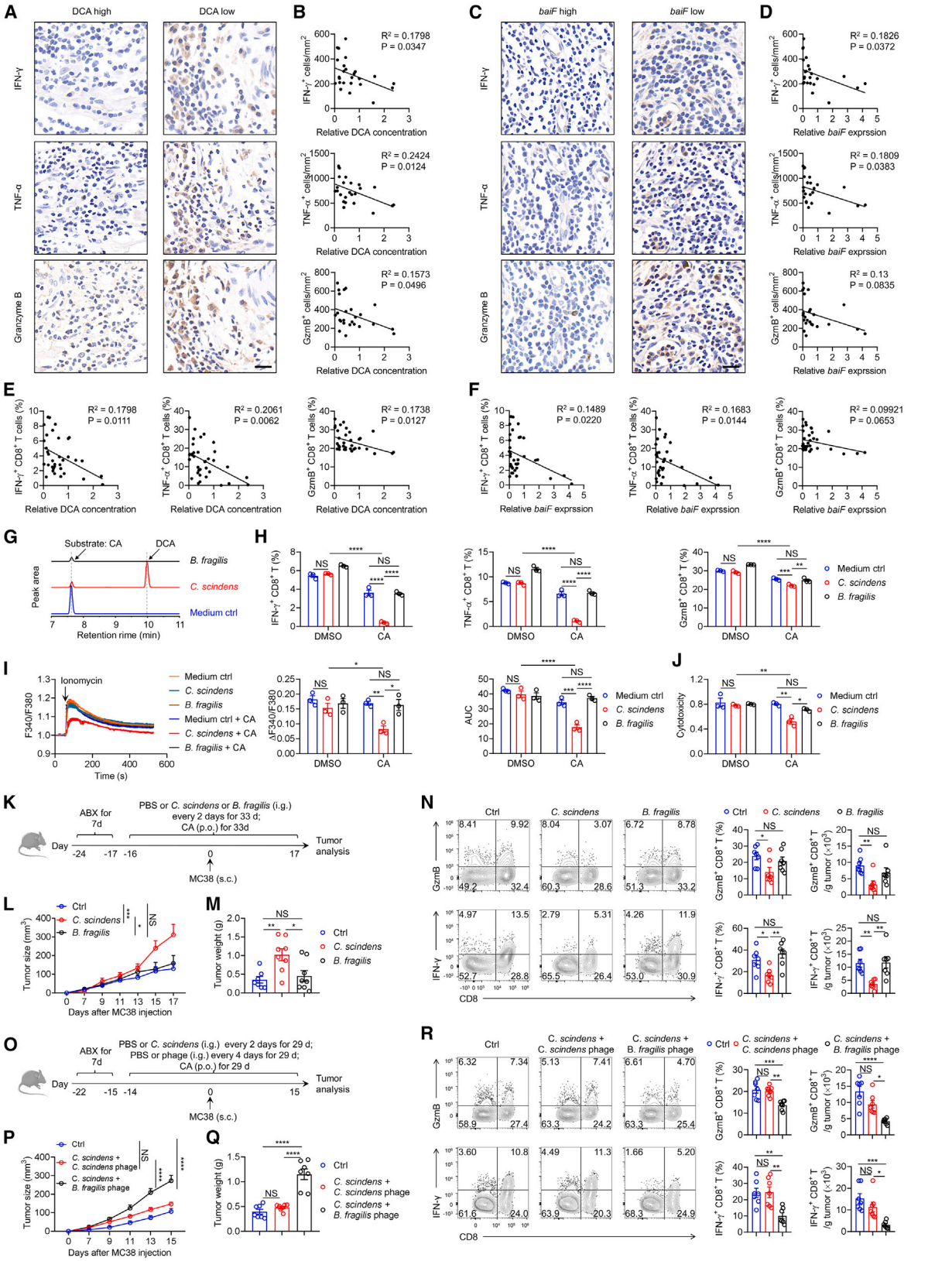

(legend on next page)

$CD4^+$ T cells expressing GzmB and IFN-γ in the DCA-exposed mice (Figures S4A and S4F). However, the exhaustion status of tumor-infiltrating $CD8^+$ T cells was not affected by DCA (Figures S4B and S4G).

The *Apc*$^{min/+}$ mice were fed with DCA-containing or normal drinking water, commencing at 6 weeks of age and continuing until 18 weeks of age (Figure 4E). DCA increased the tumor burden (Figure 4F), accompanied by impaired expression of GzmB and IFN-γ in $CD8^+$ T cells, as well as diminished expression of IFN-γ in $CD4^+$ T cells harvested from the tumor microenvironment (Figures 4G and S4L).

We next assessed the impacts of DCA on the anti-tumor responses of $CD8^+$ T cells using *in vivo* cytotoxicity assays. Briefly, B16-OVA cells and DCA-pretreated OT-1 $CD8^+$ T cells were co-injected (subcutaneously) into *Rag1*$^{-/-}$ mice, which are devoid of mature T and B cells (Figure 4H). The anti-tumor effects of antigen-specific $CD8^+$ T cells were largely inhibited by DCA treatment, in comparison to DMSO-pretreated $CD8^+$ T cells (Figures 4I and 4J), suggesting that DCA directly suppresses the cytotoxicity of tumor-localized $CD8^+$ T cells.

We compared DCA treatment of MC38-bearing WT mice or *Rag1*$^{-/-}$ mice (Figure 4K). Whereas DCA exerted a tumor-promoting effect in WT mice, it had no such impact on tumor growth in the *Rag1*$^{-/-}$ mice (Figures 4L and 4M), demonstrating a requirement for lymphocytes for DCA's tumor-promoting effects. We then injected the WT mice intraperitoneally with anti-CD8α-depleting antibody weekly to deplete $CD8^+$ T cells (Figure 4N). In the absence of $CD8^+$ T cells, DCA treatment did not exacerbate tumor growth (Figures 4O and 4P). To delineate the direct effects of DCA on $CD8^+$ T cells from any indirect influences via $CD4^+$ T cells, we performed an adoptive transfer experiment wherein splenic $CD8^+$ T cells were transferred into *Rag1*$^{-/-}$ mice that were pretreated with either DCA or PBS. Subsequently, these recipient mice were subcutaneously injected with MC38 tumor cells (Figure 4Q). DCA treatment still led to accelerated tumor growth and impaired $CD8^+$ T cell effector function (Figures 4R–4T). Taken together, these results supported that DCA promotes colorectal tumor growth by suppressing the anti-tumor $CD8^+$ T cell immune responses.

Accumulation of DCA correlates with impaired $CD8^+$ T cell effector function in patients with CRC

Intratumoral $CD8^+$ T cells exhibit a dysfunctional phenotype compared with non-tumoral $CD8^+$ T cells in CRC patients.[11–13] Moreover, serum and stool from CRC patients show increased concentrations of DCA and *bai* operon gene expression.[23,24,47] Thus, we sought to determine the potential relationships among dysfunctional anti-tumor $CD8^+$ T cell immune responses and increased DCA concentrations or *bai* operon gene expression in the CRC microenvironment. We measured fecal DCA concentrations and *bai* operon expression in CRC patients (who had not received antibiotics administration in the 2 most recent months, Table S2). Tumor sections from the same patients were assessed with immunohistochemistry (IHC) for GzmB, IFN-γ, and TNF-α. There was a negative correlation between the frequencies of effector-molecule-expressing cells and the DCA concentrations or *baiF* gene expression (Figures 5A–5D; Table S3). Additionally, we divided these CRC patients into groups based on either their DCA concentrations or their *baiF* expression: the DCA^{lo} or *baiF*^{lo} group consisted of patients with DCA concentrations or *baiF* expression ranging from the mean percentile of 0%–25%, whereas the DCA^{hi} or *baiF*^{hi} group consisted of patients with DCA concentrations or *baiF* expression ranging from the mean percentile of 75%–100%. Our data showed higher frequencies of effector-molecule-expressing cells in the DCA^{lo} group and the *baiF*^{lo} group compared with the DCA^{hi} group and *baiF*^{hi} group, respectively (Figures S5A and S5B; Table S3).

Figure 5. Accumulation of DCA correlates with impaired $CD8^+$ T cell effector function in patients with CRC

(A–D) IHC analysis of the expression of IFN-γ, TNF-α, and GzmB in tumor regions of 25 CRC patients. IFN-γ, TNF-α, and GzmB staining are shown in DCA high/low (A) and *baiF* high/low (C) tumors, scale bar, 20 μm. Correlation between the frequencies of effector molecule-expressing cells and DCA (B) or *baiF* (D) levels in CRC patients are shown; n = 25.

(E and F) Peripheral blood $CD8^+$ T cells were treated with fecal supernatants extracted from CRC patients for 24 h. Correlation between the proportions of effector molecule-expressing $CD8^+$ T cells and DCA (E) or *baiF* (F) levels are shown; n = 35.

(G) Representative LC-MS traces showing conversion of CA to DCA by *C. scindens* or *B. fragilis*.

(H) Peripheral blood $CD8^+$ T cells were treated with culture supernatants from *C. scindens* or *B. fragilis* incubated with or without CA for 24 h. Quantification of the proportions of IFN-γ^+, TNF-α^+, and $GzmB^+$ cells among $CD8^+$ T cells; n = 3. The experiment was repeated three times.

(I) Splenic $CD8^+$ T cells were treated with culture supernatants from *C. scindens* or *B. fragilis* incubated with or without CA for 24 h. Cytosolic Ca^{2+} were then measured; n = 3. The experiment was repeated twice.

(J) Splenic $CD8^+$ T cells from OT-1 mice were treated with culture supernatants from *C. scindens* or *B. fragilis* incubated with or without CA for 48 h. Scatterplots displaying the cytotoxicity of $CD8^+$ T cells against target cells; n = 3. The experiment was repeated twice.

(K) Schematic experimental procedure in (L)–(N): WT mice were fed with an antibiotic cocktail (ABX, consisting of vancomycin, neomycin, ampicillin, and metronidazole) for 7 d. The mice were then gavaged with *C. scindens* or *B. fragilis* every 2 days while being simultaneously fed with CA-containing water for 33 days and were injected (s.c.) with MC38 cells on day 0.

(L and M) Tumor growth curves (L) and tumor weight (M) at 17 days after MC38 inoculation; n = 7–8. The experiment was repeated twice.

(N) Representative flow cytometry plots and quantification of $GzmB^+$ and IFN-γ^+ cells among $CD8^+$ T cells; n = 7.

(O) Schematic experimental procedure in (P)–(R): WT mice were fed with an ABX for 7 days. The mice were then gavaged with *C. scindens* every 2 days and *C. scindens* phage or *B. fragilis* phage every 4 days while being simultaneously fed with CA-containing water for 29 days. Mice were injected (s.c.) with MC38 cells on day 0.

(P and Q) Tumor growth curves (P) and tumor weight (Q) at 15 days after MC38 inoculation; n = 7. The experiment was repeated twice.

(R) Representative flow cytometry plots and quantification of $GzmB^+$ and IFN-γ^+ cells among $CD8^+$ T cells; n = 7.

Each symbol in (M), (N), (Q), and (R) represents an individual mouse. Data are shown as mean ± SEM (H–J, L–N, and P–R). Statistics are analyzed by two-way ANOVA (H–J, L, and P) and one-way ANOVA (M, N, Q, and R); *p < 0.05, **p < 0.01, ***p < 0.001, and ****p < 0.0001. NS, not significant.

See also Figure S5 and Tables S2 and S3.

We also isolated human peripheral blood $CD8^+$ T cells from healthy volunteers, stimulated them with anti-CD3/CD28 mAbs to induce the production of effector molecules, and cultured them with supernatants extracted from the fecal samples of the aforementioned CRC patients. $CD8^+$ T cells cultured with the fecal supernatants from the patients with higher DCA concentrations or higher *baiF* expression produced less GzmB, IFN-γ, and TNF-α (Figures 5E and 5F; Table S3).

To further confirm the connection between DCA-producing bacteria, *baiF*, and anti-tumor $CD8^+$ T cell effector function in CRC, we enrolled an additional cohort of 51 CRC patients (Table S4) and obtained both fecal samples and tumor sections. Shotgun metagenomic sequencing was performed on the fecal samples of these individuals. This approach allowed for a direct quantification of the *baiF* gene. Based on the *baiF* gene expression analyzed from the shotgun metagenomics data, we divided the patients into two groups: the $baiF^{hi}$ group and the $baiF^{lo}$ group (Table S5). Through LEfSe analysis, DCA-producing bacteria *C. scindens* and *Clostridium hylemonae* (*C. hylemonae*) were enriched in the fecal samples from the $baiF^{hi}$ group (Figure S5C). Additionally, we performed IHC staining of IFN-γ and GzmB on the tumor sections from these 51 CRC patients and found decreased frequencies of cells expressing these effector molecules in the $baiF^{hi}$ group (Figure S5D; Table S5).

To test the effects of DCA-producing bacteria on $CD8^+$ T cell effector function and tumor growth, we selected two strains isolated from human fecal samples for their ability to convert CA to DCA: *C. scindens*—which can convert CA into DCA[21]; and the nontoxigenic *Bacteroides fragilis* (*B. fragilis*)—which contains incomplete *bai* operon genes and can consume CA but cannot generate DCA (Figure 5G).[17] *C. scindens* and *B. fragilis* were incubated with or without CA, and culture supernatants were added to healthy human peripheral blood $CD8^+$ T cells under stimulation with anti-CD3/CD28 mAbs. The proportions of IFN-γ^+, TNF-α^+, and $GzmB^+$ cells were decreased upon treatment with the culture supernatant of *C. scindens* with CA, as compared with those treated with the culture supernatant from *C. scindens* alone, or with the culture supernatant from *B. fragilis* with CA, or the culture medium with CA (Figure 5H). Moreover, the supernatant from *C. scindens* incubated with CA reduced cytosolic Ca^{2+} accumulation and suppressed the cytotoxicity of $CD8^+$ T cells isolated from mouse spleens (Figures 5I and 5J). Together, these data showed that DCA concentrations and *baiF* gene expression are negatively correlated with the effector function of $CD8^+$ T cells in CRC patients and also suggested that the accumulation of DCA and DCA-producing bacteria may underlie the observed impairment of $CD8^+$ T cell anti-tumor immune responses in the CRC microenvironment.

Next, mice pretreated with an antibiotic cocktail (ABX, consisting of vancomycin, neomycin, ampicillin, and metronidazole) were given *C. scindens*, *B. fragilis*, or PBS by oral gavage while being simultaneously fed with CA-containing water. These mice were then subcutaneously injected with MC38 tumor cells (Figure 5K). Colonization of mice with *C. scindens*, but not with *B. fragilis*, or cessation of ABX treatment without bacterial colonization, led to increased serum and fecal DCA concentrations, accelerated tumor growth, and impaired expression of GzmB and IFN-γ in tumor-infiltrating $CD8^+$ T cells (Figures 5L–5N, S5E, and S5F).

We further investigated whether the tumor-promoting effect of DCA-producing bacteria was indeed mediated by DCA. We isolated a lytic bacteriophage (hereafter, phage) that specifically target *C. scindens* from municipal sewage (Figure S5G). Mice pretreated with ABX were colonized with *C. scindens*, given *C. scindens* phage by oral gavage, and fed with CA-containing water (Figure 5O). The *B. fragilis* phage, which did not affect *C. scindens* (Figure S5G), was used as a negative control (Figure 5O). Administration of *C. scindens* phage, but not *B. fragilis* phage, inhibited *C. scindens* colonization, lowered DCA concentrations in both serum and stool, mitigated tumor growth, and improved anti-tumor $CD8^+$ T cell effector function (Figures 5P–5R and S5H–S5J). Metabolomics profiling showed that this treatment led to a substantial increase in CA concentrations and a notable decrease DCA concentrations in the serum when compared with *B. fragilis* phage treatment, whereas only minor alterations were observed in other bile acids such as LCA, GDCA, and TUDCA (Figure S5J). This implicated the importance of DCA in *C. scindens* colonization-enhanced tumor growth.

We colonized mice pretreated with ABX with *C. scindens* and simultaneously treated them with cholestyramine (CHO) resin, a bile acid sequestrant aimed at reducing serum DCA concentration (Figure S5K). CHO treatment decreased serum DCA concentrations, mitigated the accelerated tumor growth, and improved anti-tumor $CD8^+$ T cell effector function (Figures S5L–S5O). These findings suggested a causative role of *C. scindens*-produced DCA in the development of CRC.

Although we initially attempted to manipulate *C. scindens* to ablate the DCA biosynthetic pathway, all identified *bai*-coding Clostridia so far lack published methods for gene transfer and do not possess readily available genetic tools,[21] Instead, we chose *Faecalicatena contorta* S122 (S122), which efficiently converts CA to DCA, and its engineered counterpart S122 mut, which lacks the ability to produce DCA (Figure S5P).[48] We colonized ABX-pretreated mice with either S122 or S122 mut (Figure S5Q). As expected, mice colonized with S122 exhibited increased serum and fecal DCA concentrations, diminished anti-tumor $CD8^+$ T cell effector function, and an increase in tumor growth, when compared with the S122 mut colonized group (Figures S5R–S5U). Taken together, these findings supported the causation between microbial DCA metabolism and the anti-tumor effector function of $CD8^+$ T cells in the context of CRC.

DISCUSSION

Bile acids are able to regulate metabolism[31] and exert an influence on immune responses in macrophages, dendritic cells, monocytes, and $CD4^+$ T cells.[25,26,49–55] Here, we have shown the direct suppressive impact of DCA on $CD8^+$ T cell effector function and demonstrated that this underlies the DCA-mediated tumor promotion observed in CRC, thus broadening our understanding of the multiple effects of bile acids on different immune cell types. DCA traditionally exerts functions through interaction with receptors including GPBAR1, FXR, and VDR.[31] Here, we showed that DCA inhibits Ca^{2+}-NFAT2 signaling by potentiating PMCA activity, thereby weakening $CD8^+$ T cell effector function. This demonstrated a known receptor-independent mechanism for DCA-mediated immunomodulatory effects.

This study showed that the inhibition of PMCA by $LaCl_3$ or sh*PMCA* did not enhance the effector function of $CD8^+$ T cells in the absence of DCA (Figures 3A, 3B, and 3D). We reasoned that during T cell activation, PMCA-mediated Ca^{2+} efflux is inhibited due to PMCA-STIM1 interactions and PMCA re-distribution into areas beneath mitochondria, thereby maximizing Ca^{2+} signaling for robust T cell activation and NFAT's transcriptional activity.[56,57] Therefore, in the absence of DCA, inhibition of PMCA did not further enhance the effector function of $CD8^+$ T cells. However, when DCA was present, it amplified PMCA-mediated Ca^{2+} efflux, which was subsequently inhibited by $LaCl_3$ or sh*PMCA*, thereby abolishing the suppressive effect of DCA on $CD8^+$ T cell effector function.

Recent research has indicated that gut-derived butyrate can directly enhance the functionality of $CD8^+$ T cells, which stands in contrast to the effects of DCA.[58] Both DCA and butyrate are abundant metabolites in the colon, generated through bacterial modification of primary bile acids and bacterial fermentation of dietary fiber, respectively. The coexistence of these metabolites with opposing effects, represented by DCA and butyrate, within the colon may contribute to maintaining an optimal immune response of $CD8^+$ T cells, for immune surveillance of cancer cells and infections. In fact, an imbalance between these metabolites has been observed in CRC patients: the concentrations of DCA and its biosynthetic genes are elevated in the stool of CRC patients,[24,47] whereas the concentrations of butyrate and its producers exhibit the opposite trend.[59,60] This shift toward an immunosuppressive microenvironment could potentially underlie the development of CRC.

In summary, we demonstrated that microbial DCA suppresses cytotoxic $CD8^+$ T cell-mediated anti-tumor immune responses by activating the Ca^{2+} exporter PMCA and suggested a potential approach for the treatment and perhaps even prevention of CRC through targeting the DCA-producing bacteria.

Limitations of the study

Although this study provides insights into the connection between microbial DCA metabolism and the anti-tumor effector function of $CD8^+$ T cells in CRC, it is important to acknowledge certain limitations. First, the specific binding site of DCA on PMCA was not identified, and how DCA enhances PMCA activity remains unclear. Second, although our *in vitro* data demonstrated obvious immunosuppressive effects of DCA on $CD4^+$ T cells as observed on $CD8^+$ T cells, the reason for the weakened impact of DCA on $CD4^+$ T cells *in vivo* remains unknown. Third, it should be noted that the sample size of CRC patients included in this study was relatively small. Conducting studies with larger cohorts would be useful to validate DCA or DCA-producing bacteria as risk factor for CRC, and it would be fascinating to conduct phage-mediated targeted therapy in CRC patients with high DCA-producing bacteria in the future.

STAR★METHODS

Detailed methods are provided in the online version of this paper and include the following:

- KEY RESOURCES TABLE
- RESOURCE AVAILABILITY
  - Lead contact
  - Materials availability
  - Data and code availability
- EXPERIMENTAL MODEL AND STUDY PARTICIPANT DETAILS
  - Mice
  - Human samples
  - Cell culture
- METHOD DETAILS
  - Cell isolations
  - Flow cytometry
  - *In vitro* $CD8^+$ T cell culture and function analysis
  - *In vitro* and *in vivo* cytotoxicity assay
  - Intracellular Ca^{2+} measurement
  - Free Ca^{2+} measurement
  - Construction of expression plasmids and transfection
  - Lentivirus production and infection
  - NFAT transcriptional activity assay
  - Immunoblotting
  - Immunoprecipitation
  - SPR assay
  - ATPase activity assay
  - Electrophysiology
  - Immunohistochemistry
  - Quantitative reverse-transcriptionPCR
  - *baiF* quantification
  - Anaerobic bacterial isolation and culture
  - Bacteriophage isolation and amplification
  - $Apc^{min/+}$ model
  - Subcutaneous tumor model
  - LC-MS
  - Bile acid metabolomics assays
  - Untargeted metabolomics assays
  - Whole-genome shotgun sequencing
- QUANTIFICATION AND STATISTICAL ANALYSIS

SUPPLEMENTAL INFORMATION

Supplemental information can be found online at https://doi.org/10.1016/j.immuni.2024.02.014.

ACKNOWLEDGMENTS

We thank Zepeng Qu and Chunhua Zhou for isolating and identifying *C. scindens* and *B. fragilis*. We thank Richard A. Flavell for providing $Apc^{min/+}$, *Caspase-1*$^{-/-}$, *Caspase-11*$^{-/-}$, and *Gsdmd*$^{-/-}$ mice. We thank Yucai Wang for providing OT-1 TCR transgenic mice. We thank Taidou Hu for measuring intracellular Ca^{2+}. We thank Runzhi Li for performing SPR assay. We thank Yi Duan for helpful discussion. This work was supported by grants from the National Natural Science Foundation of China (82325025, 92374204, 82341121, 81821001 to S.Z.; 32170912, 82371828 to W.P.; and 81902908 to J.C.); the CAS Project for Young Scientists in Basic Research (YSBR-074 to R.Z., S.Z., and W.P.), and the Strategic Priority Research Program of the Chinese Academy of Sciences (XDB0490000 to W.P.).

AUTHOR CONTRIBUTIONS

J.C. and P.L. designed and performed most of the experiments and analyzed data. Z.H., J.S., and L.D. prepared the lytic bacterial phages. Z.H. and Y.Z. contributed to the whole-cell patch clamp experiment. Z.H. performed the PMCA knockdown experiments. W.Y. and L.S. performed the ATPase activity experiments. C.L. helped with the $CD8^+$ T cell metabolites screening experiments. Y.Y. analyzed the metagenomics data. F.C. helped with bacteria

engineering. C.C. helped with the intracellular Ca^{2+} measurement experiments. C.G. provided S122 and S122 mut bacteria strains. X.S. and D.L.K. analyzed the role of DCA on $CD8^+$ T cells in *Fxr* KO mice and *Vdr* KO mice. J.Y., S.W., and Y.B. collected fecal and tissue samples from CRC patients. L.Y., R.Z., X.S., L.S., L.D., and D.L.K. provided important advice and suggestions. J.C. wrote the manuscript. S.Z., W.P., and D.L.K. revised the manuscript. S.Z. and W.P. supervised the project.

DECLARATION OF INTERESTS

S.Z. is a cofounder of Ibiome Biotechnology, which studies microbial regulation of immune responses.

Received: February 24, 2023
Revised: December 10, 2023
Accepted: February 15, 2024
Published: March 12, 2024

REFERENCES

1. Trebak, M., and Kinet, J.P. (2019). Calcium signalling in T cells. Nat. Rev. Immunol. *19*, 154–169.
2. Weidinger, C., Shaw, P.J., and Feske, S. (2013). STIM1 and STIM2-mediated Ca(2+) influx regulates antitumour immunity by CD8(+) T cells. EMBO Mol. Med. *5*, 1311–1321.
3. Feske, S., Wulff, H., and Skolnik, E.Y. (2015). Ion channels in innate and adaptive immunity. Annu. Rev. Immunol. *33*, 291–353.
4. Klein-Hessling, S., Muhammad, K., Klein, M., Pusch, T., Rudolf, R., Flöter, J., Qureischi, M., Beilhack, A., Vaeth, M., Kummerow, C., et al. (2017). NFATc1 controls the cytotoxicity of $CD8^+$ T cells. Nat. Commun. *8*, 511.
5. Hogan, P.G., Chen, L., Nardone, J., and Rao, A. (2003). Transcriptional regulation by calcium, calcineurin, and NFAT. Genes Dev. *17*, 2205–2232.
6. Macian, F. (2005). NFAT proteins: key regulators of T-cell development and function. Nat. Rev. Immunol. *5*, 472–484.
7. Naito, Y., Saito, K., Shiiba, K., Ohuchi, A., Saigenji, K., Nagura, H., and Ohtani, H. (1998). CD8+ T cells infiltrated within cancer cell nests as a prognostic factor in human colorectal cancer. Cancer Res. *58*, 3491–3494.
8. Camus, M., Tosolini, M., Mlecnik, B., Pagès, F., Kirilovsky, A., Berger, A., Costes, A., Bindea, G., Charoentong, P., Bruneval, P., et al. (2009). Coordination of intratumoral immune reaction and human colorectal cancer recurrence. Cancer Res. *69*, 2685–2693.
9. Galon, J., Costes, A., Sanchez-Cabo, F., Kirilovsky, A., Mlecnik, B., Lagorce-Pagès, C., Tosolini, M., Camus, M., Berger, A., Wind, P., et al. (2006). Type, density, and location of immune cells within human colorectal tumors predict clinical outcome. Science *313*, 1960–1964.
10. Pagès, F., Berger, A., Camus, M., Sanchez-Cabo, F., Costes, A., Molidor, R., Mlecnik, B., Kirilovsky, A., Nilsson, M., Damotte, D., et al. (2005). Effector memory T cells, early metastasis, and survival in colorectal cancer. N. Engl. J. Med. *353*, 2654–2666.
11. Liang, R., Zhu, X., Lan, T., Ding, D., Zheng, Z., Chen, T., Huang, Y., Liu, J., Yang, X., Shao, J., et al. (2021). TIGIT promotes $CD8^+$T cells exhaustion and predicts poor prognosis of colorectal cancer. Cancer Immunol. Immunother. *70*, 2781–2793.
12. Taylor, E.S., McCall, J.L., Girardin, A., Munro, F.M., Black, M.A., and Kemp, R.A. (2016). Functional impairment of infiltrating T cells in human colorectal cancer. Oncoimmunology *5*, e1234573.
13. Zhang, L., Yu, X., Zheng, L., Zhang, Y., Li, Y., Fang, Q., Gao, R., Kang, B., Zhang, Q., Huang, J.Y., et al. (2018). Lineage tracking reveals dynamic relationships of T cells in colorectal cancer. Nature *564*, 268–272.
14. Sepich-Poore, G.D., Zitvogel, L., Straussman, R., Hasty, J., Wargo, J.A., and Knight, R. (2021). The microbiome and human cancer. Science *371*, eabc4552.
15. Cullin, N., Azevedo Antunes, C., Straussman, R., Stein-Thoeringer, C.K., and Elinav, E. (2021). Microbiome and cancer. Cancer Cell *39*, 1317–1341.
16. Zitvogel, L., Daillère, R., Roberti, M.P., Routy, B., and Kroemer, G. (2017). Anticancer effects of the microbiome and its products. Nat. Rev. Microbiol. *15*, 465–478.
17. Ridlon, J.M., Kang, D.J., and Hylemon, P.B. (2006). Bile salt biotransformations by human intestinal bacteria. J. Lipid Res. *47*, 241–259.
18. Wahlström, A., Sayin, S.I., Marschall, H.U., and Bäckhed, F. (2016). Intestinal Crosstalk between Bile Acids and Microbiota and Its Impact on Host Metabolism. Cell Metab. *24*, 41–50.
19. Funabashi, M., Grove, T.L., Wang, M., Varma, Y., McFadden, M.E., Brown, L.C., Guo, C., Higginbottom, S., Almo, S.C., and Fischbach, M.A. (2020). A metabolic pathway for bile acid dehydroxylation by the gut microbiome. Nature *582*, 566–570.
20. White, B.A., Lipsky, R.L., Fricke, R.J., and Hylemon, P.B. (1980). Bile acid induction specificity of 7 alpha-dehydroxylase activity in an intestinal Eubacterium species. Steroids *35*, 103–109.
21. Ridlon, J.M., Harris, S.C., Bhowmik, S., Kang, D.J., and Hylemon, P.B. (2016). Consequences of bile salt biotransformations by intestinal bacteria. Gut Microbes *7*, 22–39.
22. Bernstein, H., Bernstein, C., Payne, C.M., and Dvorak, K. (2009). Bile acids as endogenous etiologic agents in gastrointestinal cancer. World J. Gastroenterol. *15*, 3329–3340.
23. Bayerdörffer, E., Mannes, G.A., Richter, W.O., Ochsenkühn, T., Wiebecke, B., Köpcke, W., and Paumgartner, G. (1993). Increased serum deoxycholic acid levels in men with colorectal adenomas. Gastroenterology *104*, 145–151.
24. Reddy, B.S., and Wynder, E.L. (1977). Metabolic epidemiology of colon cancer. Fecal bile acids and neutral sterols in colon cancer patients and patients with adenomatous polyps. Cancer *39*, 2533–2539.
25. Campbell, C., McKenney, P.T., Konstantinovsky, D., Isaeva, O.I., Schizas, M., Verter, J., Mai, C., Jin, W.B., Guo, C.J., Violante, S., et al. (2020). Bacterial metabolism of bile acids promotes generation of peripheral regulatory T cells. Nature *581*, 475–479.
26. Song, X., Sun, X., Oh, S.F., Wu, M., Zhang, Y., Zheng, W., Geva-Zatorsky, N., Jupp, R., Mathis, D., Benoist, C., et al. (2020). Microbial bile acid metabolites modulate gut RORγ+ regulatory T cell homeostasis. Nature *577*, 410–415.
27. Matsumoto, M., Kibe, R., Ooga, T., Aiba, Y., Kurihara, S., Sawaki, E., Koga, Y., and Benno, Y. (2012). Impact of intestinal microbiota on intestinal luminal metabolome. Sci. Rep. *2*, 233.
28. Bender, M.J., McPherson, A.C., Phelps, C.M., Pandey, S.P., Laughlin, C.R., Shapira, J.H., Medina Sanchez, L., Rana, M., Richie, T.G., Mims, T.S., et al. (2023). Dietary tryptophan metabolite released by intratumoral Lactobacillus reuteri facilitates immune checkpoint inhibitor treatment. Cell *186*, 1846–1862.e26.
29. Hamilton, J.P., Xie, G., Raufman, J.P., Hogan, S., Griffin, T.L., Packard, C.A., Chatfield, D.A., Hagey, L.R., Steinbach, J.H., and Hofmann, A.F. (2007). Human cecal bile acids: concentration and spectrum. Am. J. Physiol. Gastrointest. Liver Physiol. *293*, G256–G263.
30. Benedetti, A., Alvaro, D., Bassotti, C., Gigliozzi, A., Ferretti, G., La Rosa, T., Di Sario, A., Baiocchi, L., and Jezequel, A.M. (1997). Cytotoxicity of bile salts against biliary epithelium: a study in isolated bile ductule fragments and isolated perfused rat liver. Hepatol. *26*, 9–21.
31. Fiorucci, S., and Distrutti, E. (2015). Bile Acid-Activated Receptors, Intestinal Microbiota, and the Treatment of Metabolic Disorders. Trends Mol. Med. *21*, 702–714.
32. O'Keefe, S.J., Tamura, J., Kincaid, R.L., Tocci, M.J., and O'Neill, E.A. (1992). FK-506- and CsA-sensitive activation of the interleukin-2 promoter by calcineurin. Nature *357*, 692–694.
33. Figurski, A.C. (2018). Cholelithiasis. In Integrative Medicine (Elsevier), pp. 450–456.e2.
34. Chatila, T., Silverman, L., Miller, R., and Geha, R. (1989). Mechanisms of T cell activation by the calcium ionophore ionomycin. J. Immunol. *143*, 1283–1289.

35. Bautista, D.M., Hoth, M., and Lewis, R.S. (2002). Enhancement of calcium signalling dynamics and stability by delayed modulation of the plasma-membrane calcium-ATPase in human T cells. J. Physiol. *541*, 877–894.

36. Booth, L.A., Gilmore, I.T., and Bilton, R.F. (1997). Secondary bile acid induced DNA damage in HT29 cells: are free radicals involved? Free Radic. Res. *26*, 135–144.

37. Robert, X., and Gouet, P. (2014). Deciphering key features in protein structures with the new ENDscript server. Nucleic Acids Res. *42*, W320–W324.

38. Enyedi, A., Flura, M., Sarkadi, B., Gardos, G., and Carafoli, E. (1987). The Maximal Velocity and the Calcium Affinity of the Red Cell Calcium Pump May Be Regulated Independently. J. Biol. Chem. *262*, 6425–6430.

39. Filoteo, A.G., Enyedi, A., and Penniston, J.T. (1992). The Lipid-Binding Peptide from the Plasma Membrane Ca2+ Pump Binds Calmodulin, and the Primary Calmodulin-Binding Domain Interacts with Lipid. J. Biol. Chem. *267*, 11800–11805.

40. Strehler, E.E., and Zacharias, D.A. (2001). Role of alternative splicing in generating isoform diversity among plasma membrane calcium pumps. Physiol. Rev. *81*, 21–50.

41. Tidow, H., Poulsen, L.R., Andreeva, A., Knudsen, M., Hein, K.L., Wiuf, C., Palmgren, M.G., and Nissen, P. (2012). A bimodular mechanism of calcium control in eukaryotes. Nature *491*, 468–472.

42. Kowalski, A., Betzer, C., Larsen, S.T., Gregersen, E., Newcombe, E.A., Bermejo, M.C., Langkilde, A.E., Kragelund, B.B., Jensen, P.H., and Nissen, P. (2023). Monomeric α-Synuclein activates the Plasma Membrane Calcium Pump. EMBO J. *42*, e111122.

43. Falchetto, R., Vorherr, T., Brunner, J., and Carafoli, E. (1991). The Plasma Membrane Ca2+ Pump Contains a Site That Interacts with Its Calmodulin-Binding Domain. J. Biol. Chem. *266*, 2930–2936.

44. Bonza, M.C., and Luoni, L. (2010). Plant and animal type 2B Ca2+-ATPases: Evidence for a common auto-inhibitory mechanism. FEBS Lett. *584*, 4783–4788.

45. Bonza, M.C., Luoni, L., and De Michelis, M.I. (2001). Stimulation of plant plasma membrane Ca2+-ATPase activity by acidic phospholipids. Physiol. Plant. *112*, 315–320.

46. Moser, A.R., Pitot, H.C., and Dove, W.F. (1990). A dominant mutation that predisposes to multiple intestinal neoplasia in the mouse. Science *247*, 322–324.

47. Wirbel, J., Pyl, P.T., Kartal, E., Zych, K., Kashani, A., Milanese, A., Fleck, J.S., Voigt, A.Y., Palleja, A., Ponnudurai, R., et al. (2019). Meta-analysis of fecal metagenomes reveals global microbial signatures that are specific for colorectal cancer. Nat. Med. *25*, 679–689.

48. Jin, W.B., Li, T.T., Huo, D., Qu, S., Li, X.V., Arifuzzaman, M., Lima, S.F., Shi, H.Q., Wang, A., Putzel, G.G., et al. (2022). Genetic manipulation of gut microbes enables single-gene interrogation in a complex microbiome. Cell *185*, 547–562.e22.

49. Guo, C., Xie, S., Chi, Z., Zhang, J., Liu, Y., Zhang, L., Zheng, M., Zhang, X., Xia, D., Ke, Y., et al. (2016). Bile Acids Control Inflammation and Metabolic Disorder through Inhibition of NLRP3 Inflammasome. Immunity *45*, 802–816.

50. Hao, H., Cao, L., Jiang, C., Che, Y., Zhang, S., Takahashi, S., Wang, G., and Gonzalez, F.J. (2017). Farnesoid X Receptor Regulation of the NLRP3 Inflammasome Underlies Cholestasis-Associated Sepsis. Cell Metab. *25*, 856–867.e5.

51. Hang, S., Paik, D., Yao, L., Kim, E., Trinath, J., Lu, J., Ha, S., Nelson, B.N., Kelly, S.P., Wu, L., et al. (2019). Bile acid metabolites control TH17 and Treg cell differentiation. Nature *576*, 143–148.

52. Qi, X., Yun, C., Sun, L., Xia, J., Wu, Q., Wang, Y., Wang, L., Zhang, Y., Liang, X., Wang, L., et al. (2019). Gut microbiota–bile acid–interleukin-22 axis orchestrates polycystic ovary syndrome. Nat. Med. *25*, 1225–1233.

53. Ma, C., Han, M., Heinrich, B., Fu, Q., Zhang, Q., Sandhu, M., Agdashian, D., Terabe, M., Berzofsky, J.A., Fako, V., et al. (2018). Gut microbiome-mediated bile acid metabolism regulates liver cancer via NKT cells. Science *360*, eaan5931.

54. Li, W., Hang, S., Fang, Y., Bae, S., Zhang, Y., Zhang, M., Wang, G., McCurry, M.D., Bae, M., Paik, D., et al. (2021). A bacterial bile acid metabolite modulates T_{reg} activity through the nuclear hormone receptor NR4A1. Cell Host Microbe *29*, 1366–1377.e9.

55. Paik, D., Yao, L., Zhang, Y., Bae, S., D'Agostino, G.D., Zhang, M., Kim, E., Franzosa, E.A., Avila-Pacheco, J., Bisanz, J.E., et al. (2022). Human gut bacteria produce T_H17-modulating bile acid metabolites. Nature *603*, 907–912.

56. Ritchie, M.F., Samakai, E., and Soboloff, J. (2012). STIM1 is required for attenuation of PMCA-mediated Ca2+ clearance during T-cell activation. EMBO J. *31*, 1123–1133.

57. Quintana, A., Pasche, M., Junker, C., Al-Ansary, D., Rieger, H., Kummerow, C., Nuñez, L., Villalobos, C., Meraner, P., Becherer, U., et al. (2011). Calcium microdomains at the immunological synapse: how ORAI channels, mitochondria and calcium pumps generate local calcium signals for efficient T-cell activation. EMBO J. *30*, 3895–3912.

58. He, Y., Fu, L., Li, Y., Wang, W., Gong, M., Zhang, J., Dong, X., Huang, J., Wang, Q., Mackay, C.R., et al. (2021). Gut microbial metabolites facilitate anticancer therapy efficacy by modulating cytotoxic CD8+ T cell immunity. Cell Metab. *33*, 988–1000.e7.

59. Wang, T., Cai, G., Qiu, Y., Fei, N., Zhang, M., Pang, X., Jia, W., Cai, S., and Zhao, L. (2012). Structural segregation of gut microbiota between colorectal cancer patients and healthy volunteers. ISME J. *6*, 320–329.

60. He, Y., Ling, Y., Zhang, Z., Mertens, R.T., Cao, Q., Xu, X., Guo, K., Shi, Q., Zhang, X., Huo, L., et al. (2023). Butyrate reverses ferroptosis resistance in colorectal cancer by inducing c-Fos-dependent xCT suppression. Redox Biol. *65*, 102822.

61. Langmead, B., and Salzberg, S.L. (2012). Fast gapped-read alignment with Bowtie 2. Nat. Methods *9*, 357–359.

62. Bolger, A.M., Lohse, M., and Usadel, B. (2014). Trimmomatic: a flexible trimmer for Illumina sequence data. Bioinformatics *30*, 2114–2120.

63. Li, J.H., Jia, H.J., Cai, X.H., Zhong, H.Z., Feng, Q., Sunagawa, S., Arumugam, M., Kultima, J.R., Prifti, E., Nielsen, T., et al. (2014). An integrated catalog of reference genes in the human gut microbiome. Nat. Biotechnol. *32*, 834–841.

64. Li, H., and Durbin, R. (2009). Fast and accurate short read alignment with Burrows–Wheeler transform. Bioinformatics *25*, 1754–1760.

STAR★METHODS

KEY RESOURCES TABLE

REAGENT or RESOURCE	SOURCE	IDENTIFIER
Antibodies		
FITC anti-mouse CD45.2 Antibody (104)	Biolegend	Cat#109805; RRID: AB_313442
FITC anti-mouse/human CD44 Antibody (IM7)	Biolegend	Cat#103021; RRID: AB_493684
FITC anti-mouse CD4 Antibody (GK1.5)	Biolegend	Cat#100406; RRID: AB_312691
PE anti-mouse ki67 Antibody (16A8)	Biolegend	Cat#652404; RRID: AB_2561525
PE anti-human/mouse Granzyme B Antibody (QA16A02)	Biolegend	Cat#372207; RRID: AB_2687031
PE anti-mouse CD279 (PD-1) Antibody (RMP1-30)	Biolegend	Cat#109104; RRID: AB_313421
PE anti-human/mouse TOX Antibody (TXRX10)	Thermo Fisher Scientific	Cat#12-6502-82; RRID: AB_10855034
eFluor™ 660 anti-human/mouse TOX Antibody (TXRX10)	Thermo Fisher Scientific	Cat#50-6502-82; RRID: AB_2574265
PerCP anti-mouse CD4 Antibody (GK1.5)	Biolegend	Cat#100434; RRID: AB_893324
PerCP anti-mouse CD69 Antibody (H1.2F3)	Biolegend	Cat#104522; RRID: AB_2260065
PerCP anti- human CD8a Antibody (HIT8a)	Biolegend	Cat#300909; RRID: AB_314113
PerCP anti- mouse CD45 Antibody (30-F11)	Biolegend	Cat#103130; RRID: AB_893339
PE-Cy7 anti- mouse IFN-γ Antibody (XMG1.2)	Biolegend	Cat#505826; RRID: AB_2295770
PE-Cy7 anti- mouse TCRβ Antibody (H57-597)	Biolegend	Cat#109222; RRID: AB_893625
PE/Cy7 anti-mouse CD3 Antibody (17A2)	Biolegend	Cat#100220; RRID: AB_1732057
APC anti-mouse CD279 (PD-1) Antibody (29F.1A12)	Biolegend	Cat#135210; RRID: AB_2159183
APC anti- mouse TNF-α Antibody (MP6-XT22)	Biolegend	Cat#506307; RRID: AB_315428
APC anti- mouse CD25 Antibody (PC61)	Biolegend	Cat#102011; RRID: AB_312860
APC-Cy7 anti- mouse CD8a Antibody (53-6.7)	Biolegend	Cat#100713; RRID: AB_312752
Pacific Blue anti-mouse CD3 Antibody (17A2)	Biolegend	Cat#100213; RRID: AB_493644
BV421 anti-mouse CD3e Antibody (145-2C11)	BD Biosciences	Cat#562600; RRID: AB_11153670
BV421 anti-mouse CD366 (Tim-3) Antibody (RMT3-23)	Biolegend	Cat#119723; RRID: AB_2616908
BV421 anti- mouse TCRβ Antibody (H57-597)	Biolegend	Cat#109230; RRID: AB_2562562
PE anti- human TNF-α Antibody (MAb11)	Biolegend	Cat#502908; RRID: AB_315260
PE-Cy7 anti-human TNF-α Antibody (MAb11)	BD Biosciences	Cat#557647; RRID: AB_396764
FITC anti- human IFN-γ Antibody (B27)	Biolegend	Cat#506504; RRID: AB_315437

(*Continued on next page*)

Continued

REAGENT or RESOURCE	SOURCE	IDENTIFIER
BV421 anti-human Granzyme B Antibody (GB11)	BD Biosciences	Cat#563389; RRID: AB_2738175
Ultra-LEAFTM Purified anti-mouse CD3 (172)	Biolegend	Cat#100253; RRID: AB_2810314
Ultra-LEAFTM Purified anti-mouse CD28 (37.51)	Biolegend	Cat#302934; RRID: AB_11148949
Ultra-LEAFTM Purified anti-mouse IL-4 (11B11)	Biolegend	Cat#504135; RRID: AB_2750404
Ultra-LEAFTM Purified anti-mouse IFN-γ (XMG1.2)	Biolegend	Cat#505847; RRID: AB_2616675
Ultra-LEAFTM Purified anti-human CD3 (UCHT1)	Biolegend	Cat#300438; RRID: AB_11146991
Ultra-LEAFTM Purified anti-human CD28 (CD28.2)	Biolegend	Cat#302934; RRID: AB_11148949
Mouse monoclonal anti-NFAT2	Abcam	Cat#ab2796; RRID: AB_303308
Mouse monoclonal anti-β-Actin	Proteintech	Cat#66009-1-Ig; RRID: AB_2687938
Mouse monoclonal anti-Flag M2	Sigma	Cat#F1804; RRID: AB_262044
Rabbit monoclonal anti-Phospho-Zap-70 (Tyr319)/Syk (Tyr352) (65E4)	Cell Signaling Technology	Cat#2717; RRID: AB_2218658
Rabbit monoclonal anti-Phospho-Src Family (Tyr416)	Cell Signaling Technology	Cat#2101; RRID: AB_331697
Rabbit monoclonal anti-Phospho-LAT (Tyr220)	Cell Signaling Technology	Cat#3584; RRID: AB_2157728
Rabbit monoclonal anti-Phospho-PLCγ1 (Tyr783)	Cell Signaling Technology	Cat#2821;RRID: AB_330855
Mouse monoclonal anti-Lamin B1	Proteintech	Cat#66095-1-Ig; RRID: AB_11232208
Mouse monoclonal anti-GAPDH	Proteintech	Cat#60004-1-Ig; RRID: AB_2107436
Mouse monoclonal anti PMCA4 (JA9)	NOVUS BIOLOGICALS	Cat#NB300-569; RRID: AB_2061726.
Mouse monoclonal anti pan-PMCA (5F10)	NOVUS BIOLOGICALS	Cat#NB300-578; RRID: AB_2091527
Goat anti-mouse IgG-HRP	Beyotime	Cat#A0216; RRID: AB_2860575
Goat anti-rabbit IgG-HRP	Beyotime	Cat#A0208; RRID: AB_2892644
InVivo MAb anti-mouse CD8α	BioXCell	Cat#BE0004-1; RRID: AB_1107671
Rabbit anti- GzmB	ZSGB-BIO	Cat#ZA-0599; RRID: AB_3075510
Rabbit anti-IFN-γ	Abcam	Cat#ab25101; RRID: AB_448613.
Rabbit anti-TNF-α	Servicebio	Cat#GB11188; RRID: AB_3075517
Bacterial and virus strains		
Clostridium scindens	This paper	N/A
Bacteroides fragilis	This paper	N/A
Faecalicatena contorta S122 (S122)	Wen-Bing et al., 2022[48]	N/A
C. scindens phage (CS266P1)	This paper	N/A
B. fragilis phage (BF494P2)	This paper	N/A
Biological samples		
Feces from patients with colorectal cancer	the First Affiliated Hospital of USTC and Changhai Hospital	N/A
Paraffin embedded tumor tissues of CRC patients	the First Affiliated Hospital of USTC and Changhai Hospital	N/A

(*Continued on next page*)

Continued

REAGENT or RESOURCE	SOURCE	IDENTIFIER
Chemicals, peptides, and recombinant proteins		
Fetal Bovine Serum	ThermoFisher	Cat#10091148
Penicillin-Streptomycin	Gibco	Cat#10378016
RPMI 1640 medium	ThermoFisher	Cat#22400089
Gibco™ BASIC DMEM, High Glucose,Pyruvate	Gibco	Cat#C11995500BT
SMM 293-TII Expression Medium	Sino Biological	Cat#M293TII
Glycerol	Sangon Biotech	Cat#A100854-0100
TRNzol Universal Reagent	TIANGEN	Cat#DP424
SYBR green qPCR master mix	Vazyme	Cat#Q311-02
HiScript III RT SuperMix for qPCR	Vazyme	Cat#R323-01
Red Blood Cell Lysis Buffer	Biosharp	Cat#BL503A
PBS	Thermo Fisher Scientific	Cat#10010023
Collagenase II	Sigma-Aldrich	Cat#C6885
DNase I	Roche	Cat#11284932001
biotin-labeled DCA	PeptideValley	Cat#TP-DC-19080
Ampicillin sodium	Sangon Biotech	Cat#A610028
Neomycin trisulfate salt hydrate	Sangon Biotech	Cat#A610366
Metronidazole	Sangon Biotech	Cat#A600633
Vancomycin hydrochloride	MACKLIN	Cat#V820413
Collagenase IV	Sigma-Aldrich	Cat#C5138
Percoll	Sigma-Aldrich	Cat#GE17-0891-01
Recombinant human IL-2	Peprotech	Cat#200-02
monensin	eBioscience	Cat#00-4505-51
3-oxocholic acid	Avanti	Cat#700237P
YM-58483 (BTP2)	MCE	Cat#HY-100831
Sodium glycodeoxycholate	Sigma-Aldrich	Cat#G9910
12-dehydrocholic acid	Shanghai yuanye Bio-Technology Co., Ltd	Cat#Y13544
7-oxo-deoxycholic acid	MCE	Cat#HY-41324
Taurodeoxycholate sodium salt	MCE	Cat#HY-128853
Indole-3-carboxaldehyde	MACKLIN	Cat#I811783
Cholestyramine	Sigma-Aldrich	Cat#C4650
Sodium glycodeoxycholate	aladdin	Cat#S102123
Sodium taurodeoxycholate hydrate	aladdin	Cat#S168485
Lithocholic acid	Shanghai yuanye Bio-Technology Co., Ltd	Cat#S30545
PEI transfection reagent	Polysciences	Cat#23966-1
Opti-MEM	Thermo Fisher Scientific	Cat#32985070
0.5M EDTA PH8.0	Biosharp	Cat#BL581A
HEPES	Sigma-Aldrich	Cat#H3375
Immobilon Western Chemiluminescent, HRP Substrate	Millipore	Cat#WBKLS0500
SM buffer	Gbiosciences	Cat#786-491
Ficoll	Solarbio	Cat#P8900
$LaCl_3$	Sigma-Aldrich	Cat#449830
Thapsigargin (Tg)	Sigma-Aldrich	Cat#T9033
DS16570511	MCE	Cat#HY-115595
CTV	Thermo Fisher Scientific	Cat#C34557
pluronic F-127	Beyotime	Cat#ST501

(*Continued on next page*)

Continued

REAGENT or RESOURCE	SOURCE	IDENTIFIER
Fura-2, AM	Thermo Fisher Scientific	Cat#F1201
EGTA	Sangon Biotech	Cat#A600077
streptavidin-sepharose beads	Millipore	Cat#16-126
PMA	Sigma-Aldrich	Cat#P8139
Ionomycin calcium salt	Sigma-Aldrich	Cat#I3909
Glfu Anaerobic Medium Broth	Solarbio	Cat#LA4450
BHI	Oxoid	Cat#CM1135B
L-Cysteine	Sangon Biotech	Cat#A600132-0100
HEPES	Sigma-Aldrich	Cat#H3375
BSA	Sigma-Aldrich	Cat#A1933
KeygenMax 3000 transfection reagent	KeyGEN Biotech	Cat#KGA9705
Lenti-Pac™ Lentivirus Concentration Solution	GeneCopoeia	Cat#LT007
Critical commercial assays		
MojoSort™ Mouse CD8 Naïve T Cell Isolation Kit	Biolegend	Cat#480044
MojoSort™ Mouse CD8 T Cell Isolation Kit	Biolegend	Cat#480035
MojoSort™ Human CD8 T Cell Isolation Kit	Biolegend	Cat#480012
Fixation/Permeabilization Solution Kit	BD Bioscience	Cat#554714
Cell Stimulation Cocktail (plus protein transport inhibitors)	eBioscience	Cat#00-4975-93
eBioscience™ Foxp3/Transcription Factor Staining Buffer Set	eBioscience	Cat#00-5523-00
Zombie Aqua™ Fixable Viability Kit	Biolegend	Cat#423102
Zombie NIRTM Fixable Viability Kit	Biolegend	Cat#423105
Cell Line Nucleofector® Kit V	Lonza	Cat#VCA-1003
Calcium Assay Kit (Colorimetric)	Abcam	Cat#ab102505
ATPase colorimetric Assay Kit	Abcam	Cat#ab234055
GeneJET PCR Purification Kit	Thermo Fisher Scientific	Cat#K0702
Deposited data		
Whole-genome shotgun sequencing data	NCBI BioProject ID	PRJNA1045967
Experimental models: Cell lines		
HEK293T cells	ATCC	CRL-3216
HEK293F cells	Sino Biological Inc.	N/A
MC38 cells	Lieping Chen Lab	N/A
Jurkat cells	Zhigang Tian Lab	N/A
B16-OVA cells	Jun Wang Lab	N/A
Experimental models: Organisms/strains		
C57BL/6JGpt mice	GemPharmatech	Strain NO. N000013
Rag1$^{-/-}$ mice	GemPharmatech	Strain NO. T004753
Apc$^{min/+}$ mice	Richard Flavell Lab	N/A
Caspase-1$^{-/-}$ mice	Richard Flavell Lab	N/A
Caspase-11$^{-/-}$ mice	Richard Flavell Lab	N/A
Gsdmd$^{-/-}$ mice	Richard Flavell Lab	N/A
Rip3$^{-/-}$ mice	Rongbin Zhou Lab	N/A
OT-1 TCR transgenic mice	Yucai Wang Lab	N/A
Gpbar1$^{-/-}$ mice	the Knockout Mouse Project (KOMP)	RRID: MMRRC_047915-UCD
Fxr $^{-/-}$ mice	The Jackson Lab	RRID: IMSR_JAX:004144
Vdr $^{-/-}$ mice	The Jackson Lab	RRID: IMSR_JAX:006133
Gsdme$^{-/-}$ mice	This paper	N/A

(*Continued on next page*)

Continued		
REAGENT or RESOURCE	SOURCE	IDENTIFIER
Oligonucleotides		
qPCR primers for indicated genes	This paper	See STAR Methods table
Recombinant DNA		
NFAT-luciferase reporter plasmid	YouBio	Cat#VT2046
pRL Renilla Luciferase Control Reporter Vectors	Promega	Cat#E2241
pCDNA3.3 -Flag-mPMCA4	This paper	N/A
pCDNA3.3 -Flag-hPMCA4	This paper	N/A
pCDNA3.3 -Flag-hPMCA4 (301-350)	This paper	N/A
pCDNA3.3 -Flag-hPMCA4 (1054-1205)	This paper	N/A
pCAG-hPMCA4 (301-350)-Flag	This paper	N/A
pCAG- hPMCA4 (1054-1205) -Flag	This paper	N/A
pCAG- hSERCA -Flag	This paper	N/A
psPAX2	Addgene	12260
pMD2.G	Addgene	12259
PLKO.1-GFP-shPMCA4	This paper	N/A
Software and algorithms		
FlowJo version 10	FlowJo	https://www.flowjo.com/
Image Lab 5.2.1	Image Lab	https://www.bio-rad.com/en-hk/product/image-lab-software?ID=KRE6P5E8Z
ImageJ	NIH	https://imagej.nih.gov/ij/
SnapGene 3.2.1	SnapGene	https://www.snapgene.com/
Bio-Rad CFX Manager 3.1	Bio-Rad CFX Manager	https://www.bio-rad.com/en-hk/sku/1845000-cfx-manager-software?ID=1845000
Biacore™ 8K Control Software	Cytiva	https://www.cytivalifesciences.com.cn/zh/cn/support/software/biacore-downloads
Biacore™ Insight Evaluation Software	Cytiva	https://www.cytivalifesciences.com.cn/zh/cn/support/software/biacore-downloads
Origin 2019b	OriginLab	https://www.originlab.com/
Prism version 8	Graphpad	https://www.graphpad.com/
Other		
Immobilon-P PVDF membrane	Millipore	IPVH00010
0.45-μm polyvinylidene fluoride filter	Milipore	SLHV033RB

RESOURCE AVAILABILITY

Lead contact

Further information and requests for resources and reagents should be directed to and will be fulfilled by the lead contact, Shu Zhu (zhushu@ustc.edu.cn).

Materials availability

This study did not generate new unique reagents.

Data and code availability

- The raw data of whole-genome shotgun sequencing has been deposited in the NCBI BioProject repository and processed data has been deposited using KneadData (https://www.ncbi.nlm.nih.gov/bioproject/PRJNA1045967), a procedure built upon Bowtie2[61] and Trimmomatic.[62]
- These data are publicly available as of the date of publication. Accession numbers are listed in the key resources table. Original western blot images and microscopy data reported in this paper will be shared by the lead contact upon request.
- This paper does not report an original code.
- Any additional information required to reanalyze the data reported in this paper is available from the lead contact upon request.

EXPERIMENTAL MODEL AND STUDY PARTICIPANT DETAILS

Mice

Fxr$^{-/-}$*Vdr*$^{-/-}$ mice were obtained by crossing *Fxr*$^{-/-}$ with *Vdr*$^{-/-}$ mice. *Gsdme*$^{-/-}$ mice were generated by CRISPR-Cas9 technology. Exon 2 of the *Gsdme* gene were targeted by two sgRNAs: gggtttcccaagaggctagt and gttgttccagatgtcccacc. Genotyping of *Gsdme*$^{-/-}$ mice was performed using primers: cattactgtggctaaagagggg and ggagcctagctttgaagtctaat, with amplicons of a 681-bp product from the WT allele, and a 304-bp product from the targeted allele. All mice had a C57BL/6 background and were housed in specific pathogen-free conditions. Mice were maintained under a 12-hour light-dark cycle at 23°C, and had free access to water and standard rodent diet. All experimental procedures involving mice were approved by the Ethics Committee of USTC (reference: USTCACUC202101026).

Human samples

All human samples used in the present study were obtained under the approval of the Ethics Committee of the USTC (2021KY02). Informed consent was obtained from each subject for the use of fecal samples and peripheral blood.

The fecal samples (n = 86) and paraffin embedded tumor tissues (n = 76) of CRC patients were obtained from the First Affiliated Hospital of USTC and the Changhai Hospital. Patients were selected based on the primary disease and had no treatment before fecal sample collection. Patients reporting the use of antibiotics during the 2 months before fecal sample collection were excluded from the study. The peripheral bloods were collected from 3 healthy volunteers. More patient characteristics were shown in Tables S2 and S4.

Cell culture

HEK293T and MC38 were cultured in high-glucose DMEM containing 10% FBS, 100 U/mL penicillin, and 100 μg/mL streptomycin. HEK293F cells were cultured in 293T-II medium (key resources table) containing 10% FBS, 100 U/mL penicillin, and 100 μg/mL streptomycin. Jurkat cells were cultured in RPMI-1640 containing 10% FBS, 100 U/mL penicillin, and 100 μg/mL streptomycin. All cells were maintained at 37°C in a 5% CO_2 incubator.

METHOD DETAILS

Cell isolations

For isolation of splenic lymphocytes, spleens were pressed through sieves, and lymphocytes were then obtained after lysing erythrocytes. For isolation of lymph node lymphocytes, lymph nodes were pressed through sieves, and cell suspensions were collected. For isolation of intestinal intraepithelial lymphocytes (IELs), small or large intestines were flushed thoroughly with PBS to remove contents and opened longitudinally. The small or large intestines were then cut into pieces and digested in RPMI 1640 medium with 1 mM EDTA and 2% FBS for 20 min at 37°C. Suspensions were filtered through sieves and lymphocytes were obtained by Percoll gradient centrifugation. The tumor-infiltrating lymphocytes of *Apc*$^{min/+}$ mice were isolated from the tumoral regions of small intestines as described in isolation of small intestinal IELs. For isolation of MC38 tumor-infiltrating lymphocytes, tumors were cut into pieces and digested in RPMI 1640 medium with 1 mg/mL collagenase and 20 μg/mL DNase for 40 min at 37°C. Suspensions were filtered through sieves and lymphocytes were obtained by Percoll gradient centrifugation.

For isolation of mouse CD8$^+$ T cells, cells were purified from splenic lymphocytes through magnetic activated cell sorting (MACS) using mouse CD8$^+$ T cell negative selection kits (key resources table). For isolation of human CD8$^+$ T cells, peripheral blood from healthy volunteers were loaded onto a Ficoll density gradient to obtain lymphocytes. CD8$^+$ T cells were then purified through MACS using human CD8$^+$ T cell negative selection kits (key resources table). The purity of the sorted cell populations was > 90%.

Flow cytometry

The isolated cells were incubated with anti-CD16/32 mAbs to block Fc receptors, followed by staining with fluorescence antibodies against surface molecules for 30 min at 4°C. For intracellular staining, cells were first treated with cell stimulation cocktail plus protein transport inhibitors or monensin (key resources table) for 4 h at 37°C, followed by staining for surface molecules. Cells were then fixed and permeabilized using a Fixation/Permeablization Kit (key resources table), and stained for intracellular molecules. All data were collected on a BECKMAN COULTER CytoFLEX S flow cytometer, and analyzed with Flowjo software (key resources table).

In vitro CD8$^+$ T cell culture and function analysis

To measure the effector molecules, purified CD8$^+$ T cells were stimulated with anti-CD3 and anti-CD28 mAbs in the presence of metabolites (Table S1) or bacteria supernatants for 24 h at 37°C, and monensin (2 μM) were added during the last 4 h. Cells were then harvested for detecting expressions of IFN-γ, TNF-α and GzmB by flow cytometry. In some experiments, $LaCl_3$ (60 μM), Tg (5 nM) or DS16570511 (25 μM) were added. For proliferation assay, purified CD8$^+$ T cells labeled with 2 μM of CTV were stimulated with anti-CD3/CD28 mAbs (5/2 μg/mL) and 100 U/mL IL-2 in the presence of DCA or DMSO for 72 h. Cells were then harvested, and proliferation was analyzed by CTV dilution.

In vitro and *in vivo* cytotoxicity assay

In vitro cytotoxicity of $CD8^+$ T cells was assessed using the xCELLigence Real-Time Cell Analyzer (RTCA) Multiple Plate system (ACEA Biosciences), which monitors surviving adhesive target cells every 15 min. To blank the E-Plate 16 (Roche), we placed 50 μL assay medium to each well for background measurement. B16-OVA target cells (1×10^4 cells/well) in 100 μL assay medium were added to the plate, which was then engaged into xCELLigence at 37°C. After 24 h, purified OT-1 $CD8^+$ T cells (8×10^4 cells/well) in 50 μL assay medium, which were pretreated with anti-CD3/CD28 mAbs (5/2 μg/mL) in the presence of metabolites or bacteria supernatants for 48 h at 37°C, were added to the plate and co-cultured with B16-OVA target cells for another 72 h. The cell index reflected the number of surviving target cells, and was normalized to an equal value at the time point of addition of $CD8^+$ T cells. As the control, B16-OVA cells were cultured alone to measure spontaneous death under the same condition.

To assess *in vivo* cytotoxicity of $CD8^+$ T cells, we purified OT-1 $CD8^+$ T cells, and pretreated the cells with anti-CD3/CD28 mAbs (5/2 μg/mL) in the presence of DCA or DMSO for 48 h at 37°C. After washing twice with PBS to remove DCA or DMSO, the cell counts and viability of $CD8^+$ T cells were assayed using trypan blue. A total of 3×10^5 live DCA- or DMSO-pretreated $CD8^+$ T cells were then co-injected (subcutaneously) with B16-OVA target cells (3×10^5 cells/mouse) into *Rag1*$^{-/-}$ mice. The tumor volume was monitored every 2 days, and was calculated as (width^2 × length)/2.

Intracellular Ca^{2+} measurement

Purified $CD8^+$ T cells were pretreated with anti-CD3/CD28 mAbs (5/2 μg/mL) in the presence of DCA or bacteria supernatants for 24 h at 37°C, and were loaded with Ca^{2+} indicator Fura-2, AM (2 μM) and pluronic F-127 (0.02%) in Ca^{2+}-containing Ringer's solution (which consists of 140 mM NaCl, 5 mM KCl, 2 mM $MgCl_2$, 2 mM $CaCl_2$, 10 mM HEPES, 10 mM glucose) for 30 min at 37°C, followed by washing twice with Ca^{2+}-free Ringer's solution. Cells were then resuspended in Ca^{2+}-free Ringer's solution, and Ca^{2+} measurements were performed using a calcium imaging system consisting of a DG-5 wavelength switcher (Sutter Instrument), an ORCA-Flash4.0 LT+ complementary metal oxide-semiconductor (CMOS) camera (Hamamatsu), and a Ti2 microscope (Nikon). Fura-2, AM fluorescence was measured at 510 nm after excitation at 340 nm and 380 nm every 5 s, and intracellular Ca^{2+} was determined as the F340/F380 emission ratio. To induce intracellular Ca^{2+} flux, 3 μM ionomycin was added to the cells after 60 s, and Fura-2, AM fluorescence was recorded for another 460 s. For Ca^{2+} extrusion assay, Fura-2, AM fluorescence was recorded for 60 s, and 2 μM Tg was added to depleting ER Ca^{2+} stores in the absence of extracellular Ca^{2+}. Subsequent elevation of extracellular Ca^{2+} to 1 mM led to elevated intracellular Ca^{2+}; upon reaching its peak, extracellular Ca^{2+} was again removed by addition of 3 mM EGTA to monitor intracellular Ca^{2+} decay.

Free Ca^{2+} measurement

For measurement of free Ca^{2+} in medium, DMSO, DCA (0.5 mM), $CaCl_2$ (0.5 mM) and EDTA (0.5 mM) were added to T cell culture medium, and incubated for 2 h at 37°C. The medium was collected and the concentration of free Ca^{2+} was measured using a Calcium Assay Kit (key resources table) according to manufacturer's instructions.

Construction of expression plasmids and transfection

NFAT-luciferase reporter plasmid contains an NFAT response element that drives the transcription of a firefly luciferase gene. The plasmids were co-transfected with the *Renilla* luciferase plasmid (pRLTK) that controls for cell viability and transfection efficiency. pLVX-mCherry was used to construct ΔCaM-AI by cloning into the cDNA encoding a deletion mutant of the C-terminal autoinhibitory domain of the calcineurin catalytic subunit, which leads to a constitutive, Ca^{2+}-independent phosphatase activity. These plasmids were transfected into Jurkat cells using a Nucleofector Kit (key resources table) for Jurkat cells. After 24 h, the transfected cells were stimulated with PMA/ionomycin (0.08/1.3 μM) in the presence of 150 μM DCA or DMSO for 24 h, followed by immunoblotting, qPCR, and luciferase assays.

For immunoprecipitation, Flag-PMCA4, which contains a Flag-tag at N terminus, was generated by inserting PCR-amplified PMCA4 (human: GenBank: NM_001684.5, mouse: Genbank: NM_213616.4) immediately after Flag within a pcDNA3.3 vector. HEK293T cells were transfected with cloned pcDNA3.3 plasmids using PEI transfection reagent (key resources table). For ATPase activity assay, truncations of the human PMCA4, including deleting residues 301-350 and C-terminal residues 1054-1205 of PMCA4 were generated by a standard two-step PCR using the synthetic gene. The full-length SERCA (Genbank: NM_005173.4), PMCA4 and truncated constructs were cloned into pCAG vector with a C-terminal Flag-tag.

Lentivirus production and infection

The targeting sequence for human PMCA4 (Genbank: NM_001684.5) is as follows (5′ to 3′): CCCTTGATTTAGTTCCAGAAT. To produce lentivirus, a PLKO.1-GFP vector encoding shRNA specific to the target molecule was co-transfected with psPAX2 and pMD2.G into HEK293T cells at a mass ratio of 2:2:1. The transfection reagent used was KeygenMax 3000 (key resources table). The medium was replaced after 6 h. At 48 h post transfection, supernatants were collected and filtered through a 0.45 μm filtration system. The viral supernatants were concentrated using Lenti-Pac™ Lentivirus Concentration Solution (key resources table) according to the manufacturer's protocol. For Jurkat cells, viral infection was performed using spin-infection at 300 rpm at 37°C for 2 h with 10 μg/mL polybrene. Lentiviral-infected cells were sorted using a BD FACSAria III cell sorter. The knockdown of target proteins was confirmed by immunoblot analysis.

NFAT transcriptional activity assay

After PMA/ionomycin (0.08/1.3 μM) stimulation, the Jurkat cells co-transfected with NFAT-luciferase reporter plasmids and pRLTK were collected, and both firefly and *Renilla* luciferase activity were measured using a dual luciferase assay system. The firefly luciferase activity was normalized to the *Renilla* luciferase activity. In some experiments, ΔCaM-AI or empty vector was co-transfected with NFAT-luciferase reporter plasmids and pRLTK.

Immunoblotting

Cells were collected, and lysed in Noidet P-40 (NP-40) lysis buffer with protease inhibitors (cOmplete Tablets EDTA-free and PMSF) on ice for 30 min. The target protein was separated by SDS-PAGE and transferred to polyvinylidene fluoride (PVDF) membranes, followed by blockade with 5% bovine serum albumin (BSA) for 30 min at room temperature. PVDF membranes were probed with primary antibodies overnight, and then probed with secondary antibodies conjugated to horseradish peroxidase (HRP) for 1 h at room temperature. The following antibodies were used: mouse anti-NFAT2, mouse anti-β-actin, rabbit anti-phospho-Zap-70 (Tyr319)/Syk (Tyr352), rabbit anti-phospho-PLCγ1 (Tyr783), rabbit anti-phospho-LAT (Tyr220), rabbit anti-phospho-Src family (Tyr416), mouse anti-Flag, rabbit anti-LaminB, mouse anti-GAPDH, HRP goat anti-mouse IgG, HRP goat anti-rabbit IgG (key resources table). The ratios of nuclear NFAT2 to cytosolic NFAT2, p-Src to β-actin, p-Zap70 to β-actin, p-LAT to β-actin, and p-PLCγ1 to β-actin were quantified through densitometric analysis using ImageJ software. These values were presented in arbitrary units. To ensure comparability, the relative ratios were normalized to their respective control groups.

Immunoprecipitation

HEK293T cells transfected with Flag-PMCA4b or empty vector were harvested and resuspended in 500 μL ice-cold IP buffer (25 mM Tris-HCl, PH7.4, 150 mM NaCl, 1 mM EDTA, 1% NP-40, 5% glycerol) containing protease inhibitors. Cells were lysed on ice for 30 min, and lysates were cleared by centrifugation. One-tenth of the volume of the lysate was set aside to be used as the input control. The remaining lysates were incubated with 1 mM biotin-labeled DCA (key resources table) or biotin and gently rotated at 4°C for 1 h, and were then incubated with streptavidin-sepharose beads (key resources table) at 4°C for 1 h. After five washes with IP buffer, proteins bound to beads were eluted using loading buffer.

SPR assay

The binding kinetics and affinity of bile acids to hPMCA4 were analyzed by SPR with running buffer HBS-EP (10 mM HEPES [pH 7.4], 150 mM NaCl, 3 mM EDTA, and 0.5% [v/v] surfactant P20) at 25°C. hPMCA4 was diluted to 20 μg/mL in HBS-EP buffer, and was covalently immobilized to a CM5 sensor chip via amine groups in 10 mM sodium acetate buffer (pH 4.5) for a final RU around 23000. Bile acids were serially diluted (from 6.25 to 0.09765625 μM) and injected onto a sensor chip at a flow rate of 30 μL/min for 120 s (contact phase), followed by 360 s of buffer flow (dissociation phase). The binding kinetics were analyzed using 1:1 binding model with the software Biacore™ Insight Evaluation software (key resources table) and stead-state analysis of data at equilibrium.

ATPase activity assay

ATPase activities of PMCA4 and SERCA were measured using the ATPase colorimetric Assay Kit (key resources table) in 96-well plates at OD_{650} nm. Briefly, 3 μg protein was added in the reaction buffer consisting of 25 mM HEPES-KOH, pH 7.4, 150 mM KCl, 10 mM $MgCl_2$ and 0.01% DDM to 100 μL as one reaction sample. Reactions were performed at 37°C for 10 min, and the amount of released Pi was then quantitatively measured using the ATPase colorimetric Assay Kit. The control groups in the absence of proteins were subtracted as background for each data points.

Electrophysiology

Jurkat cells were cultured on a glass coverslip, and then transferred into an external bath solution of 130 mM NaCl, 5 mM KCl, 1 mM $MgCl_2$, 2.5 mM $CaCl_2$, 10 mM HEPES, and 10 mM glucose, pH 7.4. Borosilicate glass pipettes were filled with internal solution containing 140 mM KCl, 10 mM NaCl, 1 mM $CaCl_2$, 1 mM $MgCl_2$, 11 mM EGTA and 10 mM HEPES. Whole-cell patch clamp recordings were performed using Axopatch 200B patch-clamp amplifier (Molecular Devices) linked to a personal computer equipped with Digidata 1550B data acquisition system (Molecular Devices). After seal formation, the membrane beneath the pipette was ruptured and the pipette solution was allowed to dialyze into the cell for 10–15 min before recording the resting membrane potential in current-clamp mode. After achieving a stable current recording for approximately ten minutes, add either DMSO or DCA to continue monitoring changes in current-clamp mode. Data were analyzed with Clampfit 10.7 (Molecular Devices) and OriginPro 2019 (OriginLab).

Immunohistochemistry

Paraffin-embedded tissues from CRC patients were sectioned longitudinally at 5 μm. Before staining, the sections were de-waxed and rehydrated, followed by heat-induced antigen retrieval. Afterwards, the sections were incubated in 0.3% H_2O_2 for 20 min for blockade of endogenous peroxidase, and were then incubated in blocking buffer (goat serum) for 30 min. Primary and secondary antibodies were added, followed by counterstaining with hematoxylin. The following primary antibodies were used: rabbit anti-GzmB, rabbit anti-IFN-γ, and rabbit anti-TNF-α (key resources table).

Quantitative reverse-transcriptionPCR

Total RNA was extracted and purified from cells using TRIzol reagent and was transcribed to cDNA using HiScriptIII RT-SuperMix for qPCR according to manufacturer's instructions. qPCR was performed using ChamQ SYBR qPCR Master Mix (key resources table) on the CFX384 Real-Time System, and primer pairs used for target genes are listed below:

RT-qPCR primers	IDENTIFIER
hIFN-γ-Forward: TCGTTTTGGGTTCTCTTGGCT	N/A
hIFN-γ-Reverse: GGACATTCAAGTCAGTTACCGAA	N/A
hTNF-α-Forward: CTCTTCTGCCTGCTGCACTTTG	N/A
hTNF-α-Reverse: ATGGGCTACAGGCTTGTCACTC	N/A
hRpl13a-Forward: CGAGGTTGGCTGGAAGTACC	N/A
hRpl13a-Reverse: CTTCTCGGCCTGTTTCCGTAG	N/A
16S-Forward: AGAGTTTGATCMTGGCTCAG	N/A
16S-Reverse: CTGCTGCSYCCCGTAG	N/A
S122-Forward: ACTAAGAAGCCCCGGCTAAC	Wen-Bing et al., 2022[48]
S122-Reverse: TTCGACAGTTTCCAATGCAG	Wen-Bing et al., 2022[48]
C. scindens-Forward: TGACGGTACYYNRKGAGGAAGCC	N/A
C. scindens-Reverse: ACTACGGTTRAGCCGTAGCCTTT	N/A
B. fragilis-Forward: CGAGGGGCATCAGGAAGAA	N/A
B. fragilis-Reverse: CGGAATCATTATGCTATCGGGTA	N/A
BaiF-Forward: TTCAGYTTCTACACCTG	N/A
BaiF-Reverse: *GGTTRTCCATRCCGAACAGCG*	N/A

baiF quantification

Fecal samples were collected from mice or CRC patients, and were stored at -80°C before processing. DNA was extracted from fecal samples with GeneJET PCR Purification Kit (key resources table) according to the manufacturer's instructions, and normalized to 2 ng/μL. To quantify *baiF* relative to the total bacterial DCA in a sample, qPCR was performed for the 16S rRNA and *baiF* genes using genomic DNA as templates.

Anaerobic bacterial isolation and culture

C. scindens and *B. fragilis* were isolated from human fecal samples. Briefly, fecal samples were diluted with PBS and seeded onto agar plates (YCFA, which consists of 1 g/L casitone, 2.5 g/L yeast extract, 4 g/L $NaHCO_3$, 1 g/L cysteine, 0.45 g/L K_2HPO_4, 0.9 g/L NaCl, 0.09 g/L $MgSO_4 \cdot 7H_2O$, 0.09 g/L $CaCl_2$, 1 mg/L resazurin, 10 mg/L haemin, 10 μg/L biotin, 10 μg/L cobalamin, 30 μg/L p-amino-benzoic acid, 50 μg/L folic acid and 150 μg/L pyridoxamine, 0.5 mg/L thiamine, 0.5 mg/L riboflavin, 2 g/L glucose, 2 g/L maltose, 2 g/L cellobiose, 33 mM acetate, 9 mM propionate, 1 mM isobutyrate, 1 mM isovalerate, and 1 mM valerate). After culture under strictly anaerobic conditions (80% N_2, 10% H_2, and 10% CO_2) in an anaerobic chamber at 37°C for 2 - 4 days, we picked individual colonies, and performed 16S rRNA gene sequencing with universal primers (16S-27F: agagtttgatcmtggctcag, 1492R: tacggytaccttgttacgactt) to enable taxonomic characterization.

C. scindens and *B. fragilis* were grown in Glfu Anaerobic Medium Broth. The bacteria were cultured under strictly anaerobic conditions (80% N_2, 10% H_2, and 10% CO_2) at 37°C in an anaerobic chamber. In some experiments, CA (1.5 mM) was added.

Bacteriophage isolation and amplification

Phage against *C. scindens* (named CS266P1) were isolated from human fecal samples. Phage against *B. fragilis* (named BF494P2) were isolated from municipal sewage. Briefly, municipal sewage was centrifuged at 5000 rpm for 10 min at 4°C to remove any remaining solids. Human fecal samples were first resuspended with SM buffer (200 mM NaCl, 16 mM $MgSO_4$ and 0.1 M Tris-HCl, PH7.4), and centrifuged at 5000 rpm for 10 min at 4°C to remove any remaining solids. The supernatant was then sequentially filtered through a 0.8 μm and a 0.2 μm PVDF filter. The processed samples were cocultured with *C. scindens* or *B. fragilis* for three times. After the third round of enrichment, the supernatant was centrifuged at 12000 rpm for 10 min at 4°C, and filtered through a 0.22 μm PVDF filter. 500 μL of a culture of *C. scindens* or *B.fragilis* grown overnight was mixed with 4.5 mL of BHI top agar (0.4% agar) and poured onto the surface of a BHI agar plate (1.5% agar). 2.5 μL of enriched droplets was spotted onto the bacterial overlay plate to detect the presence of the phages. After overnight growth at 37°C, the resulting plaques were recovered using a sterile pipette tip in 500 μL SM buffer. Phages were purified three times by the double-layer plate method to ensure that the phages were clonal isolates.

High-titer phage stocks were generated by adding 2 mL of the above phage to 5 mL *C. scindens* or *B. fragilis* culture and then added to 45 mL BHI culture medium. After overnight growth at 37°C, the lysates were centrifuged at 12000 rpm for 10 min at 4°C. Supernatant was filtered through a 0.22 μm membrane filter and then measured the phage titer.

Apc$^{min/+}$ model

Gender-matched *Apc*$^{min/+}$ mice (6w) were randomly divided into 2 groups: Ctrl group and DCA group. The mice in Ctrl group were fed with normal sterile drinking water, and the mice in DCA group were fed with DCA-containing sterile drinking water (0.2% w/v) and refreshed every 3 days throughout the experiment. After 18 w, the mice were sacrificed, and the small intestinal tissues were obtained for analysis of tumors and $CD8^+$ T cells.

Subcutaneous tumor model

5×10^5 MC38 cells were subcutaneously (s.c.) injected into the axilla of mice (male, 6–8 weeks) on day 0. The tumor volume was calculated as ($width^2 \times length$)/2. At the experimental end points, mice were sacrificed for tumor analysis. For DCA treatment, mice were given 2.5 mM DCA daily by oral gavage or intraperitoneal injection throughout the experiment, starting from day -14. For $CD8^+$ T cell depletion experiment, mice were given intraperitoneally (i.p.) 200 μg of anti-CD8α-depleting antibody (key resources table) weekly, starting from day -1.

For colonization with *C. scindens* or *B. fragilis*, mice were fed with an antibiotic cocktail (ABX, consisting of vancomycin, neomycin, ampicillin, and metronidazole) for 1 w to deplete intestinal bacteria. The mice were then gavaged with 10^9 *C. scindens* or *B. fragilis* every 2 days throughout the experiment. Where indicated, the mice were given 8×10^9 PFU of *C. scindens* phage or *B. fragilis* phage by oral gavage every 4 days. On day 0, the mice were injected (s.c.) with MC38 cells. For CHO treatment experiment, the mice in the CHO group were fed with CHO-containing food (2.5%, w/w), while the vehicle group was fed with normal food. For colonization with S122 or S122 mut, mice were fed with an ABX for 1 w. The mice were then gavaged with 10^9 S122 or S122 mut every 2 days throughout the experiment, and were injected (s.c.) with MC38 cells on day 0.

In all bacterial colonization experiments, CA-containing water (2.s5 mM) was provided to all mice starting from the day of bacterial colonization and continued until the experimental endpoints.

LC-MS

For the treatment of fecal samples, 30 mg fecal samples were homogenized in 200 μL of prechilled ultrapure water using a homogenizer. Then, 800 μL of prechilled methanol/acetonitrile (1:1, V/V) was added and thoroughly mixed by vortexing. The mixture underwent ultrasonication for 10 min. Liquid nitrogen was then used to quench the sample for 1 min, followed by melting at room temperature. This ultrasonication and quenching process was repeated three times. The resulting mixture was incubated at −20°C for 4-6 h to facilitate protein precipitation. Afterward, centrifugation was performed at 13,000 rpm for 15 min at 4°C.

For treatment of serum samples, 30 μL serum samples were reconstituted in 120 μL of cold extraction solvent methanol/acetonitrile (1:1, V/V). The mixture was adequately vortexed and subjected to ultrasonication for 10 min. It was then incubated at −20°C for 4-6 h to precipitate proteins. Following this, centrifugation was performed at 13,000 rpm for 15 min at 4°C. The resulting supernatant was then transferred to LC vials.

Bile acid quantification was conducted using either an AB ExionLCTM Liquid Chromatography system coupled to an AB 5600+ TripleTOF system or a Shimadzu LC-MS-MS-8050. In the case of the AB ExionLCTM system, separation was achieved using an XBridge BEH C18 column (100 mm × 2.1 mm i.d.; 2.5 μm). The mobile phase consisted of solvent A (0.1% formic acid, 10 mM acetic acid amine in water) and solvent B (0.1% formic acid in 80% methanol and 20% acetonitrile). The gradient flow started at 35% B for 0.5 min, linearly increased to 60% B over the next 2.5 min, further linearly increased to 80% B over the subsequent 7 min, and then linearly increased to 90% B over the following 6 min. It was then linearly decreased to 35% B within the next 4.5 min and maintained at this composition for an additional 2.5 min. Injection volumes were 5 μL for fecal and serum samples, and 1 μL for standards and supernatant of bacteria. The analysis was performed in negative-ion mode, and data processing was done using Peak View 2.2 software based on m/z values and sample retention time.

Alternatively, when employing the Shimadzu LC-MS-MS-8050 system, separation was conducted on a Waters ACQUITY UPLC C18 column (100 mm × 2.1 mm, 1.7μm), with solvent A (5 mM acetic acid amine in water) and solvent B (acetonitrile) as the mobile phase. The gradient flow began at 10% B for 3 min, linearly increased to 60% B over the next 2 min, linearly increased to 90% B over

the subsequent 4 min and kept for 1 min. It was then linearly decreased to 10% B within the next 0.5 min, and finally maintained at this composition for an additional 3 min. The flow rate was set at 300 μL/min, the column temperature was maintained at 35°C, and the injection volume was 1 μL. The mass spectrometer operated in a negative ion mode.

Bile acid metabolomics assays

30 μL of serum samples were reconstituted in 120 μL of cold extraction solvent methanol/acetonitrile (2:1, V/V, containing 1mM BHT, CA-d4, Lyso PC17, GCA-C13 and L-2-chlorophenylalanine) to precipitate protein. The mixture was adequately vortexed and subjected to ultrasonication for 5 min. Subsequently, centrifugation was carried out at 12,000 rpm for 10 min at 4°C. From the resulting supernatant, 50 μL was taken and diluted twice with 50 μL of deionized water. The final samples were transferred to LC vials.

Bile acids were quantified with an AB Sciex Qtrap 5500/Nexera UHPLC LC-30A system. Separation was performed on a Phenomenex Kinetex C18 column (2.1mm × 100 mm, 2.6 μm) utilizing a gradient of solvent A (0.1% formic acid) and solvent B (0.1% formic acid in methanol/acetonitrile/isopropanol, 1:1:1, V/V/V). The gradient flow started at 20% B for 0.5 min, linearly increased to 38% B over the next 1 min, linearly increased to 50% B over the next 10.5 min, linearly increased to 95% B over the next 5.5 min and kept for 1.5 min, linearly decreased to 20% B over the next 0.1 min, and finally maintained at this composition for an additional 1 min. The flow rate was set at 450 μL/min, the column temperature was maintained at 45°C, and the injection volume was 5 μL. The mass spectrometer operated with a voltage of 5.5 kV in positive mode and 4.5 kV in negative mode. The ESI source conditions were set as follows: ion source gas1 at 55, ion source gas2 at 55, and source temperature at 450°C.

Untargeted metabolomics assays

80 mg human fecal samples were reconstituted in 1 mL cold extraction solvent methanol/acetonitrile/H2O (2:2:1, v/v/v), adequately vortexed, incubated on ice for 20 min, and centrifuged at 14,000 g for 20 min at 4°C. Supernatants were collected and flowed through a 96-well protein precipitation plate, and then the elution was collected and dried in a vacuum centrifuge at 4°C. For LC-MS analysis, the samples were re-dissolved in 100 μL acetonitrile/water (1:1, v/v) solvent and transferred to LC vials.

For untargeted metabolomics of polar metabolites, extracts were analyzed using a quadrupole time-of-flight mass spectrometer (Sciex TripleTOF 6600) coupled to hydrophilic interaction chromatography via electrospray ionization in Shanghai Applied Protein Technology Co., Ltd. LC separation was on a ACQUIY UPLC BEH Amide column (2.1 mm × 100 mm, 1.7 μm particle size (waters, Ireland) using a gradient of solvent A (25 mM ammonium acetate and 25 mM ammonium hydroxide in water) solvent B (acetonitrile). The gradient flow was set at 85% B for 1 min, linearly reduced to 65% in 11 min, and then was reduced to 40% in 0.1 min and kept for 4 min, and then increased to 85% in 0.1 min, with a 5 min re-equilibration period employed. Flow rate was 400 μL/ min, column temperature was 25°C, auto sampler temperature was 5°C, and injection volume was 2 μL. The mass spectrometer was operated in both negative ion and positive ionizations mode. The ESI source conditions were set as follows: Ion Source Gas1 as 60, Ion Source Gas2 as 60, curtain gas as 30, source temperature: 600°C, IonSpray Voltage Floating ± 5500 V. In MS acquisition, the instrument was set to acquire over the m/z range 60-1000 Da, and the accumulation time for TOF MS scan was set at 0.20 s/spectra. In auto MS/MS acquisition, the instrument was set to acquire over the m/z range 25 - 1000 Da, and the accumulation time for product ion scan was set at 0.05 s/spectra. The product ion scan is acquired using information dependent acquisition with high sensitivity mode selected. The parameters were set as follows: the collision energy was fixed at 35 V with ± 15 eV; declustering potential, 60 V and −60 V; exclude isotopes within 4 Da, candidate ions to monitor per cycle: 10.

Whole-genome shotgun sequencing

Fecal samples were collected from 51 CRC patients. Whole-genome shotgun sequencing of fecal samples was performed on the Illumina NovaSeq 6000 platform. The metagenomic samples underwent quality control using KneadData (https://bitbucket.org/biobakery/kneaddata), a procedure built upon Bowtie2[61] and Trimmomatic.[62] Reads of low quality and those aligning to the human (hg37_and_human_contamination) reference database were discarded. Subsequently, high-quality reads were aligned to the integrated gene catalog (IGC), which encompasses 9.9 million non-redundant microbial genes,[63] through BWA mem[64] (Version: 0.7.17-r1188) with default parameters. Alignments exceeding 50bp in length, possessing > 95% sequence identity, were selectively retained. For each gene present in the IGC, its Reads Per Kilobase per Million mapped reads (RPKM) value was calculated by dividing the gene's read count by the total read count and the gene's length. The *bai* gene hits file (provided by Li and Durbin,[64] *bai* gene against IGC gene) facilitated the determination of bai gene abundance for each metagenomic sample. Differentially abundant microbial species were identified using linear discriminant analysis effect size (LEfSe).

QUANTIFICATION AND STATISTICAL ANALYSIS

Data are presented as means ± SEM. Statistical analyses were performed using Prism 8.0 (GraphPad version 8). Specifically, two-tailed unpaired t-test between two groups, one-way analysis of variance (ANOVA) and two-way ANOVA across multiple groups were used to determine significance. For time-course analysis of tumor size, two-way ANOVA was used. The correlations between CD8 effector molecules and DCA concentration or *baiF* expression were analyzed using linear regression. Statistical parameters were represented in the Figure Legend of each Figure. $P < 0.05$ was considered significant. *$p < 0.05$, **$p < 0.01$, ***$p < 0.001$, and ****$p < 0.0001$.